AD-E 300 791

54

LEVEL

12

DNA 4498F

ADA085576

CALCULATIONS OF SRI INTERNATIONAL MX TRENCH EXPANSION AND VENTING EXPERIMENTS

Physics International Company

2700 Merced Street

San Leandro, California 94577

1 March 1978

Final Report for Period 18 July 1977—31 December 1977

CONTRACT No. DNA 001-77-C-0299

DTIC
ELECTE
JUN 1 8 1980
S
C

Prepared for

Director

DEFENSE NUCLEAR AGENCY

Washington, D. C. 20305

80 4 28 124

Destroy this report when it is no longer
needed. Do not return to sender.

REPORT DOCUMENTATION PAGE		READ INSTRUCTIONS BEFORE COMPLETING FORM
1. REPORT NUMBER DNA 4498F	2. GOVT ACCESSION NO. AD-A085576	3. RECIPIENT'S CATALOG NUMBER
4. TITLE *(and Subtitle)* CALCULATIONS OF SRI INTERNATIONAL MX TRENCH EXPANSION AND VENTING EXPERIMENTS		5. TYPE OF REPORT & PERIOD COVERED Final Report for Period 18 Jul 77—31 Dec 77
		6. PERFORMING ORG. REPORT NUMBER PIFR-1102-1
7. AUTHOR(s) D. L. Orphal M. S. Chawla K. R. Abbott		8. CONTRACT OR GRANT NUMBER(s) DNA 001-77-C-0299
9. PERFORMING ORGANIZATION NAME AND ADDRESS Physics International Company 2700 Merced Street San Leandro, California 94577		10. PROGRAM ELEMENT, PROJECT, TASK AREA & WORK UNIT NUMBERS Subtask J24AAXYX955-05
11. CONTROLLING OFFICE NAME AND ADDRESS Director Defense Nuclear Agency Washington, D.C. 20305		12. REPORT DATE 1 March 1978
		13. NUMBER OF PAGES 78
14. MONITORING AGENCY NAME & ADDRESS*(if different from Controlling Office)*		15. SECURITY CLASS *(of this report)* UNCLASSIFIED
		15a. DECLASSIFICATION/DOWNGRADING SCHEDULE

16. DISTRIBUTION STATEMENT *(of this Report)*

Approved for public release; distribution unlimited.

17. DISTRIBUTION STATEMENT *(of the abstract entered in Block 20, if different from Report)*

19. KEY WORDS *(Continue on reverse side if necessary and identify by block number)*

MX	Jet Penetration
MX Trench	Shock Wave
Trench Venting	Shock Tubes
	Theoretical Calculations

20. ABSTRACT *(Continue on reverse side if necessary and identify by block number)*

Three calculations were performed corresponding to Tests 11, 17, and 18 of
the SRI International "Laboratory Investigations of the Expansion and Venting
of the MX Trench" program. Based on analyses of the SRI International exper-
imental data and the results of several preliminary calculations (not reported
here), a new model for trench venting was developed. The new venting model is
based on simple jet penetration theory.

20. ABSTRACT (Continued)

The theoretical results show good overall agreement with the experimental data. In particular, the in-trench pressure histories and trench expansion results for the Test 18 calculation, incorporating the new venting model, agree well with the experimental data. Although further calculations and analyses are required to investigate the applicability and limitations of the venting model, the good agreement between the theoretical and experimental results for Test 18 is encouraging.

PREFACE

Accession For

NTIS GRA&I	☑
DDC TAB	☐
Unannounced	☐
Justification	

By

Distribution/

Availability Codes

| | Avail and/or |
| Dist | special |

A

Conversion factors for U.S. customary to metric (SI) units of measurement.

To Convert From	To	Multiply By
angstrom	meters (m)	1.000 000 X E -10
atmosphere (normal)	kilo pascal (kPa)	1.013 25 X E +2
bar	kilo pascal (kPa)	1.000 000 X E +2
barn	meter^2 (m^2)	1.000 000 X E -28
british thermal unit (thermochemical)	joule (J)	1.054 350 X E +3
calorie (thermochemical)	joule (J)	4.184 000
cal (thermochemical)/cm^2	mega joule/m^2 (MJ/m^2)	4.184 000 X E -2
curie	giga becquerel (GBq)*	3.700 000 X E +1
degree (angle)	radian (rad)	1.745 329 X E -2
degree Fahrenheit	degree kelvin (K)	$\tau_K = (t°\ f + 459.67)/1.8$
electron volt	joule (J)	1.602 19 X E -19
erg	joule (J)	1.000 000 X E -7
erg/second	watt (W)	1.000 000 X E -7
foot	meter (m)	3.048 000 X E -1
foot-pound-force	joule (J)	1.355 818
gallon (U.S. liquid)	meter^3 (m^3)	3.785 412 X E -3
inch	meter (m)	2.540 000 X E -2
jerk	joule (J)	1.000 000 X E +9
joule/kilogram (J/kg) (radiation dose absorbed)	Gray (Gy)**	1.000 000
kilotons	terajoules	4.183
kip (1000 lbf)	newton (N)	4.448 222 X E +3
kip/inch^2 (ksi)	kilo pascal (kPa)	6.894 757 X E +3
ktap	newton-second/m^2 (N-s/m^2)	1.000 000 X E +2
micron	meter (m)	1.000 000 X E -6
mil	meter (m)	2.540 000 X E -5
mile (international)	meter (m)	1.609 344 X E +3
ounce	kilogram (kg)	2.834 952 X E -2
pound-force (lbf avoirdupois)	newton (N)	4.448 222
pound-force inch	newton-meter (N·m)	1.129 848 X E -1
pound-force/inch	newton/meter (N/m)	1.751 268 X E +2
pound-force/foot^2	kilo pascal (kPa)	4.788 026 X E -2
pound-force/inch^2 (psi)	kilo pascal (kPa)	6.894 757
pound-mass (lbm avoirdupois)	kilogram (kg)	4.535 924 X E -1
pound-mass-foot^2 (moment of inertia)	kilogram-meter^2 (kg·m^2)	4.214 011 X E -2
pound-mass/foot^3	kilogram/meter^3 (kg/m^3)	1.601 846 X E +1
rad (radiation dose absorbed)	Gray (Gy)**	1.000 000 X E -2
roentgen	coulomb/kilogram (C/kg)	2.579 760 X E -4
shake	second (s)	1.000 000 X E -8
slug	kilogram (kg)	1.459 390 X E +1
torr (mm Hg, 0° C)	kilo pascal (kPa)	1.333 22 X E -1

*The becquerel (Bq) is the SI unit of radioactivity; 1 Bq = 1 event/s.
**The Gray (Gy) is the SI unit of absorbed radiation.

A more complete listing of conversions may be found in "Metric Practice Guide E 380-74," American Society for Testing and Materials.

CONTENTS

ILLUSTRATIONS

ILLUSTRATIONS (cont.)

ILLUSTRATIONS (cont.)

SECTION 1

INTRODUCTION

Recently SRI International (SRI) performed a series of scale model experiments in support of the MX trench concept (Reference 1). The objective of these experiments was to investigate trench expansion and venting under known and controllable conditions. The SRI experiments provide an excellent data base against which the results of calculations may be compared.

Reported here are the essential results from three calculations corresponding to SRI Tests 11, 17 and 18. The calculations were performed with the objectives of comparing the theoretical results with the experimental data and using these correlations to improve theoretical modeling of the trench expansion and venting process. As a result of this effort, a new model of trench venting was developed and is proposed for consideration.

SECTION 2

COMPUTATIONAL SETUP

The calculations of the SRI trench expansion and venting experiments Nos. 11, 17 and 18 were performed using the PISCES 1DL one-dimensional Lagrangian continuum mechanics computer code.

2.1 EXPERIMENT GEOMETRY

In the SRI trench expansion and venting experiments (Reference 1) the driver consisted of a steel shock tube section 12 feet in length with an inner diameter of 6 inches and an outer diameter of 9 inches. Eleven foot strands of primacord were suspended in the center of the driver. The source end was closed by a steel plate. The other end of the driver was connected to a 30-inch section of steel pipe (6 inches i.d., 9 inches o.d.) which acted as a run-up section for the shock. The driver and run-up sections were acoustically isolated. Attached to the other end of the run-up section was the 12-inch long trench test section.

In Test 11 the test section was composed of a piece of clay drain pipe, having a 6-inch i.d. and a 1-inch wall thickness. The density of the clay pipe was 1.92 g/cc. The pipe had two longitudinal saw cuts 0.9 inch deep. Each saw cut was offset 45 degrees from the crown. Covering the clay pipe was 2 inches of dry Monterey sand (ρ = 1.59 g/cc) and 0.5 inch of Dolomite (ρ = 1.60 g/cc).

8

In Tests 17 and 18, the test section was composed of a 3/4-inch thick steel fiber reinforced concrete pipe (ρ = 1.92 g/cc) having an inner diameter of 6 inches. The pipe had two longitudinal saw cuts, each offset from the crown by 55 degrees. The concrete pipe was covered by 2¼ inches of desert alluvium* (ρ = 1.96 g/cc) and 1/8 inch of Dolomite (ρ = 1.60 g/cc).

The entire experimental assembly was placed in a 16-foot long soil bin, that was 3-feet high and 4-feet wide.

The end of the test section was closed by a thick steel plate. A 2-inch thick lucite window in this reflecting wall facilitated photography of the tunnel expansion after shock arrival. Pressure gages were placed at the reflecting wall and 15.5 inches and 38.5 inches upstream from the reflecting wall in Tests 17 and 18. The 38.5-inch gage was not used on Test 11. Movement of the trench "roof" was monitored by means of 6 pins. These pins protruded through the soil and rested on the crown piece of the trench. The pins were located 1, 3, 5, 7, 9 and 11 inches back from the reflecting wall.

2.2 CALCULATIONAL GEOMETRY, ZONING AND BOUNDARY CONDITIONS

The computations were performed in 1½-dimensional flume symmetry (i.e., variable cross-sectional flow area). The basic computational geometry and finite difference zoning is shown in Figure 1.

In the experiments, the driver and run-up sections were made of steel pipe having a wall thickness of 1½ inches. There was no significant expansion of these sections in the experiment and the driver and run-up sections were modeled as rigid in the calculations. The concrete (or clay in Test 11) pipe test section

---
*The soil was obtained from the HAVE HOST test site at the Luke-Yuma Bombing and Gunnery Range where larger-scale trench tests were being conducted.
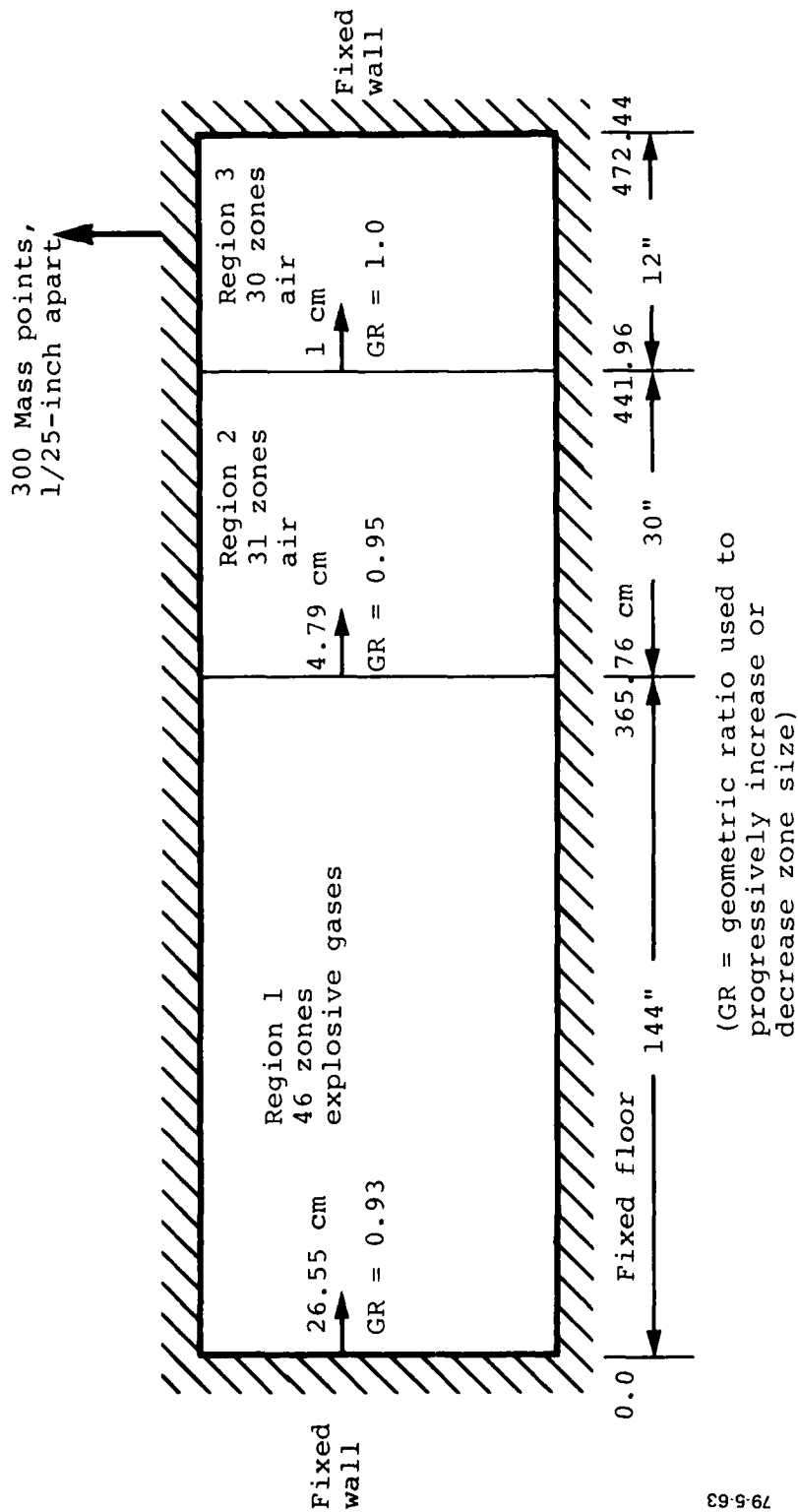
Figure 1   Geometry and finite difference zoning used for computations of SRI trench expansion and venting experiments 11, 17 and 18.

underwent considerable expansion in the experiments. In the calculations, the motion of the "roof" of the test section was described by means of 300 mass points, spaced 1/25 inch apart. The velocity of each roof mass point was calculated by employing Newton's second law of motion, the force on the mass points being the overpressure associated with the in-trench gases. The masses of all the roof points were equal and represented the overburden of a rectangular pipe whose cross-sectional area and height were respectively equal to the cross sectional area and diameter of the circular pipe of the experiment. The areal density (GMCC) associated with each mass point was calculated by using the relation:

$$GMCC = \rho_1 h_1 + \rho_2 h_2 + \rho_3 h_3$$

where ρ_1, ρ_2 and ρ_3 are the densities of concrete, Monterey sand and Dolomite, and h_1, h_2 and h_3 are their respective thicknesses.

For Tests 17 and 18, the value of GMCC was 15.5 g/cm^2 while in Test 11 the value was 14.98 g/cm^2. Figure 2 is a schematic of the cross-section geometry employed in the computations.

Although the mass points monitor the trench expansion only in the upward direction, in the early part of the calculations the sidewalls and the floor were displaced outward by an amount equal to the roof displacement. This simulates the one-dimensional symmetric expansion of the trench in the interval between the initial application of the internal pressure pulse and the arrival at the trench of the reflected stress wave from the free surface.

At the time-of-arrival at the trench of the stress wave reflected from the free surface, movement of the trench walls and floor was specified to cease and the position of the trench walls and floor was held fixed for the remainder of the calculation.
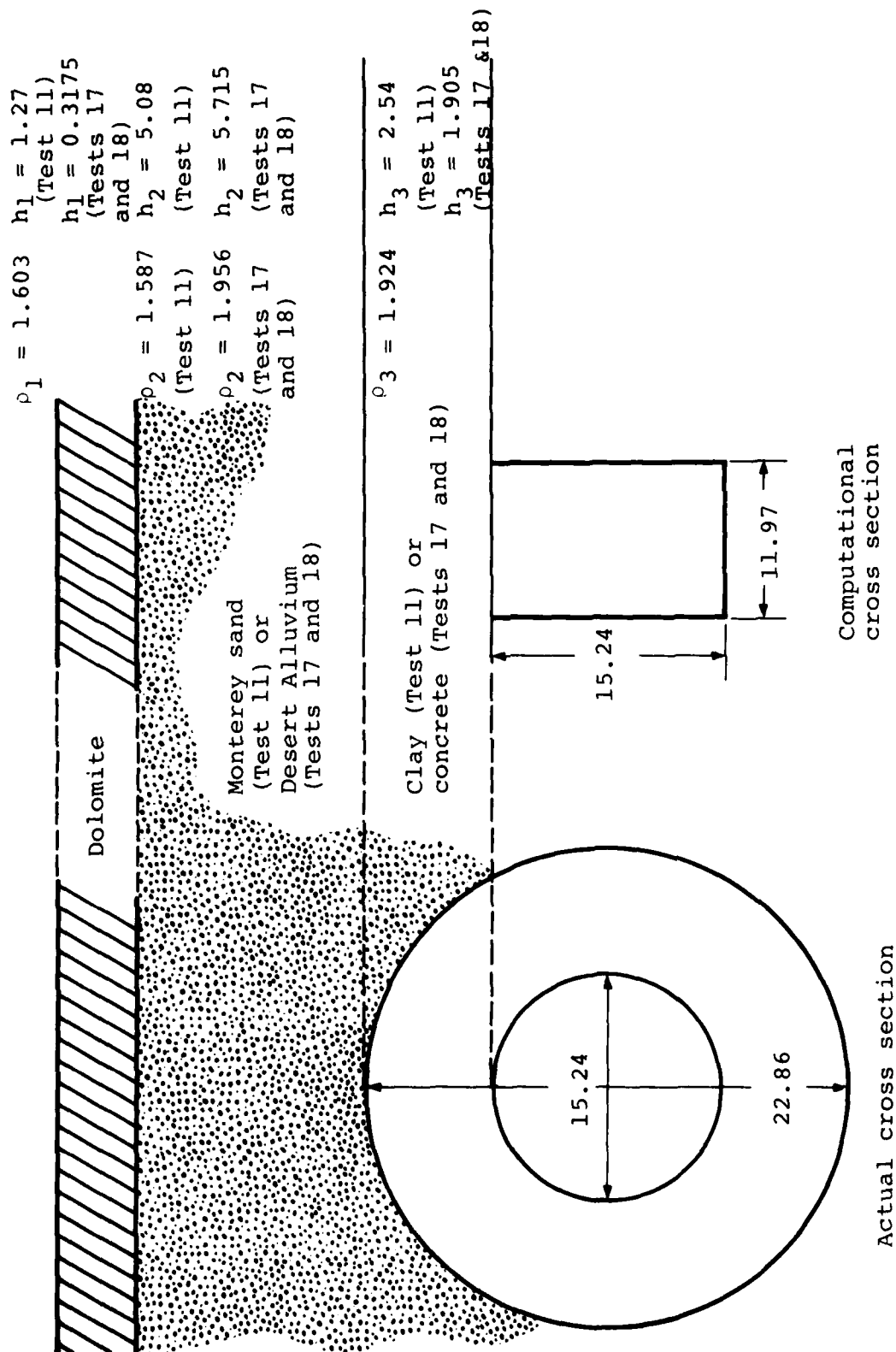
Figure 2   Schematic of actual and computational trench cross sections for the SRI trench expansion and venting experiments 11, 17 and 18. (Dimensions and densities are cm and g/cm³.)

12

For each calculation, the time-of-arrival of the free surface
reflection at the trench was specified on the basis of the SRI
experimental data. For Test 11 this time was 1166 µs after first
motion of the trench. In Test 17 and 18 this time was specified
as 1042 µs after first motion of the trench.

Of course, the arrival of the free surface reflection at the
trench only initiates the departure of trench expansion from one-
dimensional symmetry. The "walls" and "floor" of the trench do
not really cease moving at this time, but continue to move out-
ward. However, the overall expansion of the trench is now
predominantly upwards. The SRI experimental data show this
phenomenon very well (see Figure 3). Thus, the modeling procedure
described above is only an approximation to the more complicated
three-dimensional motion of the trench.

2.3 MATERIAL MODELS

The air in the trench was modeled using a tabular real air
equation-of-state (i.e., variable γ).

The trench walls and overburden soil were modeled using
discrete mass points. Thus only the inertial properties of these
materials were included in the calculations.

2.4 INITIAL CONDITIONS

The initial conditions for the air in the run-up and test
sections were:

$$V = 1 = \rho_o/\rho$$

$$\rho_o = 0.001293 \text{ g/cc}$$

$$E = 2.5 \times 10^{-6} \text{ Mbar-cc/cc}$$

$$\dot{R} = 0 \text{ cm/µs}$$

t = 0 ms

t = 1.96 ms

t = 2.55 ms

t = 3.05 ms

t - 3.54 ms

t = 4.03 ms

MP-6307-30A

Figure 3   HYCAM pictures (end view, Test 18).

14

These values corresponded to an initial γ of 1.4 and an initial pressure of 1 bar.

The treatment of the primacord burn in the driver section presented some difficulties. The primacord occupied only a small portion of the driver section volume. The remainder of the driver section was occupied by ambient air. Several simplifications were required in order that the burning of the primacord and the subsequent expansion of the primacord gases and the mixing of these gases with air could be modeled in a one-dimensional manner.

In the calculations it was assumed that the driver section was completely filled with the expanded primacord gases and air. The density and the energy of the homogeneously dispersed primacord gases corresponded respectively to the total mass of the primacord and the total energy of the PETN in the primacord.

For example, in SRI test 18, the driver section contained 8 strands of 100 gr/ft primacord. Each strand was 11-feet long; thus, the total charge consisted of 8800 grains of PETN. The linear density of the primacord (the explosive as well as the wrapper) was 9.73 g/ft (Reference 2). Thus the total primacord mass was 856.24 grams. The mass of the air in the explosive section was 86.269 grams. The density of the explosive products (i.e., primacord gases plus air) was then 0.01413 g/cc.

As noted above, the energy density, E, of the explosive products, was obtained by assuming that the pure PETN (E = 0.101 Mbar-cc/cc) (Reference 3) was uniformly dispersed throughout the driver section. Therefore for Test 18

$$E = \left(\frac{0.101 \text{ Mbar-cc}}{cc}\right)\left[\frac{(8800 \text{ gr})(0.06486 \text{ g/gr})}{\pi(7.62 \text{ cm})^2 (365.76 \text{ cm})(1.77 \text{ g/cc})}\right]$$

$$E = 4.822 \times 10^{-4} \text{ Mbar cc/cc}$$

15

The values of ρ_o and E for Tests 11 and 17 are, respectively, 0.0091 g/cc and 2.44 x 10^{-4} Mbar-cc/cc.

The equation-of-state of the homogenized explosive products was modeled using the JWL equation-of-state for PETN (Reference 3). Since the primacord products were modeled as initially highly expanded, the JWL equation-of-state was effectively reduced to a constant γ-law gas equation-of-state with $\gamma = 1.25$.

A simplification was also made regarding the time dependent burning of the primacord. In the calculations "burning" of the primacord was modeled as the time-phased release of the primacord energy in the homogeneously dispersed primacord gases. The burning of the primacord was specified to occur at a rate of 0.83 cm/μs which is the detonation speed of pure PETN. Burning of the primacord was initiated at the rear of the driver section.

Since, in effect, the modeling of the primacord burn in the driver section incorporated the highest possible detonation velocity and implicitly assumed instantaneous mixture of the primacord gases and air following detonation, it was expected that the calculated shock time-of-arrival in the run-up and test sections would be somewhat earlier than observed experimentally. This indeed was the case (see Sections 3, 4 and 5). Also contributing to the difference between the calculated and observed shock arrival times, was the fact that in the calculations the primacord gases were modeled as mixed throughout the 12-foot long driver section, whereas in the experiment the length of the primacord strands was only 11 feet.

2.5 TRENCH VENTING

A new model of trench venting was developed for use in the calculations of the SRI trench expansion and venting experiments. This trench venting model is based on an analysis of the phenomena observed in the SRI experiments.

Figure 3 is a series of HYCAM photographs at the end of the trench in SRI Test 18 (Reference 2). Shortly after arrival of the in-trench shock at the time of about 1500 µs, uniformly spaced cracks appeared about the circumference in the concrete trench. These cracks provided passages for leakage of the in-trench gases. The weakest points in the trench roof were the two pre-sawed notches, at 55 degrees from the vertical. The trench failed at these notches forming a "roof panel" and a "bottom portion" of the trench. The roof panel cracked near the crown, resulting in two upward moving "sub-panels." These sub-panels moved approximately radially outward and the area of the opening at the crown increased with time.

A gas jet was associated with each of the cracks in the trench. With the exception of the jet associated with the crown crack, the gas jets appeared to penetrate the surrounding soil only a very small distance and then essentially remained "steady state" for the times of interest. The gas jet associated with the crown crack, however, grew in length until it penetrated the overburden, at which time flow of the in-trench gases to the atmosphere began (Figures 3 and 4). This venting of the in-trench gas to the atmosphere reduced the pressure in the trench. Venting began at or near the reflecting wall and progressed upstream with time.
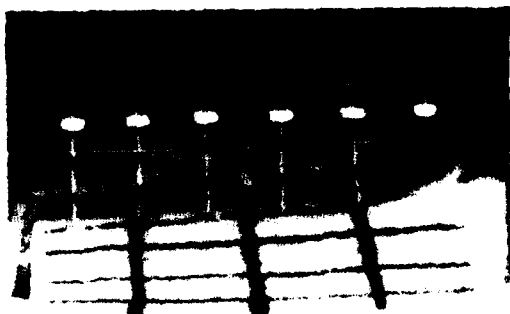
The venting model used in the calculations was based directly on the phenomenological observations made above. The model requires determination of three parameters:
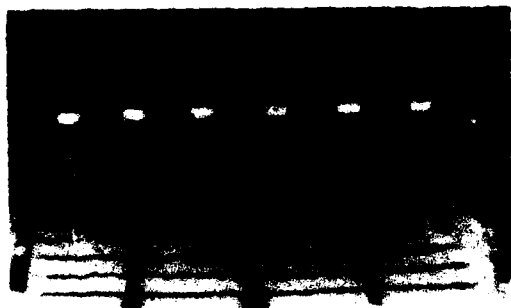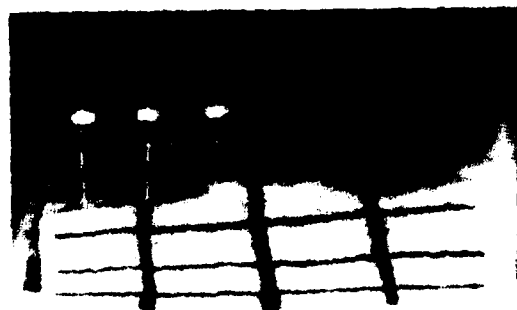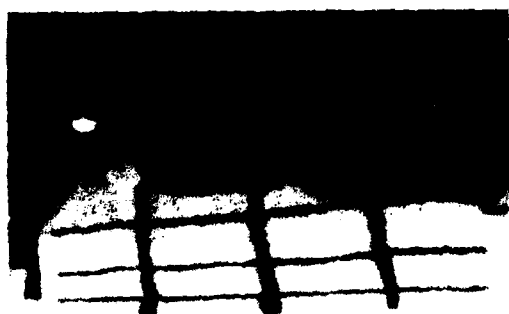
t = 0 ms   t = 2.51 ms

t = 2.80 ms   t = 3.09 ms

t ≈ 3.38 ms   t = 3.66 ms

MP-6307-31A

Figure 4   HYCAM pictures (side view, Test 18).

79-5-66

18

1. The time at which fracture of the concrete trench occurs,

2. The rate of penetration of the "crown jet" through the overburden soil, or the time at which venting begins, and,

3. The time-dependent flow area through which the in-trench gases vent to the atmosphere following penetration of the overburden soil by the crown jet

Specification of the time when fracture of the concrete trench occurs is based on an analysis of the response of the trench to a static internal pressure. The tensile strength of the concrete pipe employed in Tests 17 and 18 was about 900 psi (62 bars). The static internal pressure that will result in a hoop stress of 62 bars may be calculated using the equation (Reference 4):

$$\sigma_{\theta\theta}(r) = \left(\frac{a^2}{b^2-a^2}\right)\left(1 + \frac{b^2}{r^2}\right) P$$

where a and b are respectively the internal and external radii of the cylindrical pipe. Setting $r = a = 3$ inches, $b = 3.75$ inches, and $\sigma_{\theta\theta} = 62$ bars, and solving for the pressure, one obtains $p = 12.4$ bars. This is nearly the same as the incident shock pressure in SRI Test 17 and significantly less than the 20 bar incident shock pressure for Test 18. However, in all cases, the peak pressure associated with the reflected shock exceeded 12.4 bars.

Another consideration is the observation, noted above, that in all the SRI tests in which venting occurred, venting began at or very near the reflecting wall and progressed upstream (Reference 1). Neither this observation, the SRI experimental data, or the simple static analysis outlined above, however, provides sufficient information to specify the time when fracture of the concrete trench occurs. An assumption is therefore required. For the venting model used in the calculations, it was assumed that fracture of the concrete trench occurred upon arrival of the reflected in-trench shock.

19

An examination of the SRI HYCAM photographs of Tests 17 and 18 (Reference 2), suggests that penetration of the soil overburden is accomplished by a narrow sheet of gas that flows out of the crack(s) along the crown of the trench roof panel (Figures 3 and 4). The gases escaping through the crown crack appear to penetrate the soil overburden in much the same manner as the jet resulting from a lined explosive charge perforates a metal target. Based on this phenomenological observation, the rate at which the crown jet penetrates the soil overburden is computed from jet penetration theory.

Using simple jet penetration theory (Reference 5), the jet penetration speed, U, is given by

$$U = \frac{V}{1 + \sqrt{\rho_{soil}/\rho_{jet}}}$$

Then the parameter of interest, the time required for the gas jet to penetrate the soil overburden, T, is just

$$T = \frac{h_2 + h_3}{U}$$

where in the above equations, V is the velocity of the jet gases escaping the trench, ρ_{soil} is the soil density, ρ_{jet} is the density of the jet gas, and $(h_2 + h_3)$ is the thickness of the overburden to be penetrated (see Figure 2). The jet velocity V is assumed to be equal to the critical velocity $C_* = \sqrt{2/(\gamma+1)}\ C_o$, where C_o is the sound speed in the jet material (Reference 6).

After the soil overburden has been penetrated by the gas jet, the in-trench gases vent to the atmosphere through the newly established opening. The motion of the gases escaping through such an orifice is very complicated in general. However, for the

20

computational model, this orifice flow was simplified by assuming that the velocity of the gas flow through the opening in the critical velocity, C_*, given above. Then, the mass of in-trench gases that vents into the atmosphere through an area, Δs, in a time interval Δt is given by (Reference 6):

$$\Delta m = C_* \rho_* \ \Delta s \ \Delta t$$

In the above equation, C_* and ρ_* are the critical velocity and critical density of the gas*. The critical velocity is given above. The critical density is given by

$$\rho_* = \left(\frac{2}{\gamma+1}\right)^{1/\gamma-1} \rho_o$$

The flow area, Δs, is an increasing function of time and is modeled on the basis of the trench geometry and the assumption that the outward motion of the roof sub-panels is radial. Then the crack width is given by (see Figure 5):

$$\Delta s = 2\theta_o \ (\overline{R} - \overline{R}_o)$$

where $2\theta_o$ is the initial angular separation of the two notches defining the roof panel of the trench and $\overline{R}_o$ and $\overline{R}$ are the trench radii at the initial and the current times, respectively.

Several additional assumptions are made in the trench venting model:

1. It is assumed that only one gas jet, the jet near the crown, penetrates the soil overburden. In several of the SRI tests, including Test 17, it appears that the trench roof cracked in several places and more than one jet penetrated the soil overburden. This phenomenon is not modeled since in general it requires some means of predicting the number and location of cracks in the trench roof panel.

---

*The gas is either air or high explosive products, whichever is at the position of the "vent." 21
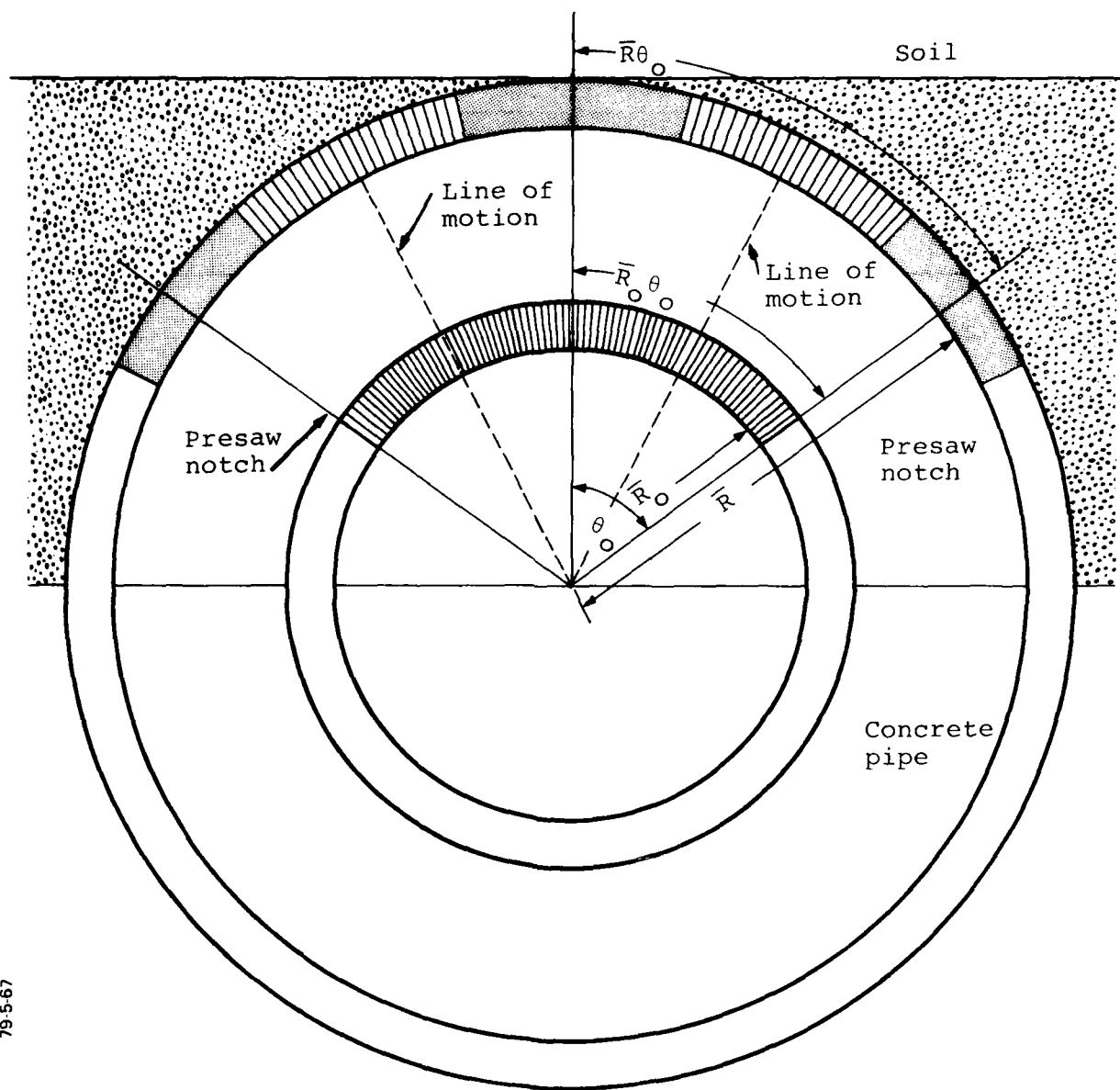
Figure 5   Schematic of radial expansion model for the trench roof sub-panels and the time-dependent flow area of the crown crack.

2. It is assumed that the total mass of the in-trench gas contained in all the jets prior to overburden penetration is negligible compared to the mass of the gas in the trench. Thus, no flow of gas from the trench is computed until the crown jet penetrates to the free surface and the trench gas may flow to the atmosphere.

3. The basic jet penetration theory employed in the model assumes that the jet material is incompressible.

SECTION 3

COMPUTATIONAL RESULTS FOR TEST 11

In SRI Test 11, 8 strands of 50 grain/foot primacord were
employed as the energy source in the driver section. Nominally
this amount of primacord corresponded to an overall initial mass
density of 0.0091 g/cc and an initial energy density of 2.44 x
10^{-4} Mbar-cc/cc in the driver section. However, when these
initial values were used in the calculation, the computed pressure
pulse in the run-up section (15.5 inches from the test section
reflecting wall) was significantly higher than observed in the
SRI experiment. In order to obtain an incident pressure pulse
amplitude that corresponded to the SRI measured pressure at the
15.5-inch-gage location, it was necessary to reduce the energy
density in the driver section to 0.75 of the nominal value (i.e.,
$E = 1.83$ x 10^{-4} Mbar-cc/cc). A similar reduction in internal
energy density was required to match the incident pressure pulses
measured in Tests 17 and 18 (see Sections 4 and 5). The reasons
for this requirement to reduce the initial energy density in the
driver to achieve the measured incident pressure are not clear.
In terms of generating a shock, certainly some energy losses
occur in the experiment; for instance there is heat loss to the
driver walls. Probably most important, however, is the energy
lost in heating the primacord wrapper material.

The experimental data for Test 11, which involved a 1-inch
thick clay pipe trench, showed no fracture in the trench. Therefore,
the trench venting model was not applied in this calculation.

24

In SRI Test 11, two gages were located in the test section reflecting wall and one gage was located in the run-up section, 15.5 inches upstream from the reflecting wall. The experimental pressure histories are reproduced in Figure 6 (Reference 7).

With the reduction of initial energy density in the driver section as described above, the computed pressure pulse at the 15.5-inch location agrees reasonably well with the measured pressure at early times. Figure 7 shows a comparison of the computed and measured pressure histories at this location. For this comparison, the experimental trace (see Figure 6) was hand digitized and consequently smoothed. Also the times-of-arrival of the measured and computed waveforms were forced to correspond. At this location, the computed time of arrival was actually about 300 µs earlier than measured (see Section 2).

As can be seen from Figure 7 the approximate 12 to 13 bar incident pulse is matched reasonably well by the calculations. The computed peak reflected pressure also agrees reasonably well with the measured value.

At times greater than about 3 ms, the experimental pressures are significantly less than those computed. This disagreement between the computed and measured pressures at this gage location is not well understood, but may be related to upstream gas leakage and heat losses in the experiment.

Figure 8 shows a comparison of the computed and measured pressure histories at the reflecting wall for Test 11. The agreement between the observed and computed peak pressure is good as is the general character of the waveform. At times greater than about 2.5 ms, the computed pressures are slightly higher than observed but there is reasonably good agreement between the calculation and experiment in terms of the pressure attenuation late time.

25
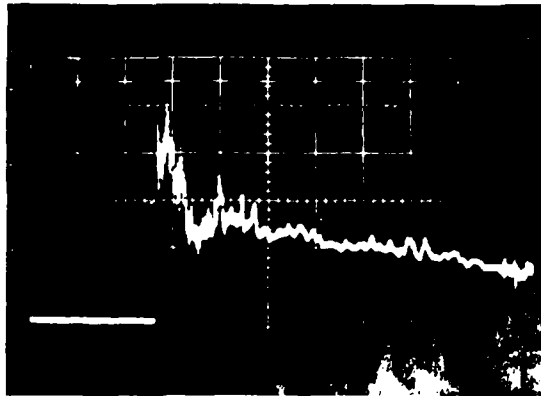
P1 (at reflecting wall)
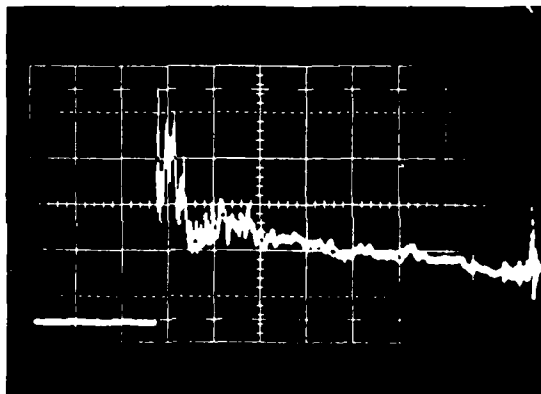
P2 (at reflecting wall)
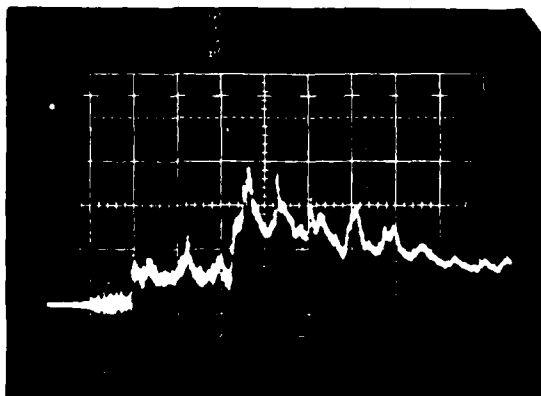
P6 (15.5 in. from reflecting wall)

Figure 6   Experimental pressure records from SRI Test 11.
250 psi per div, 500 μsec/div, 500 μsec delay
time from T_o, charge 400 gr/ft), (Reference 7).

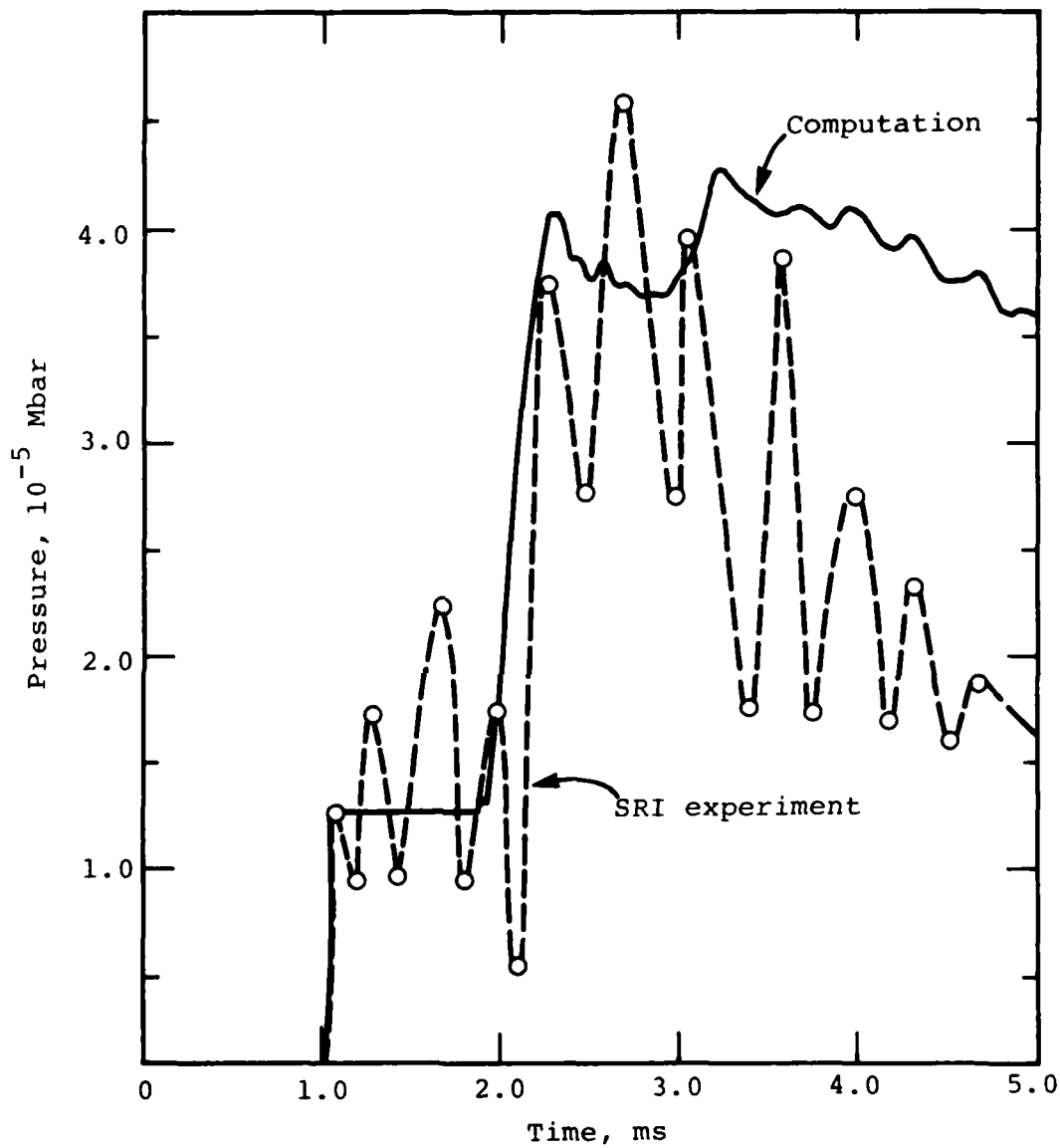**Figure 7** Comparison of computed and measured pressure histories at 15.5 inches from the reflecting wall, Test 11.
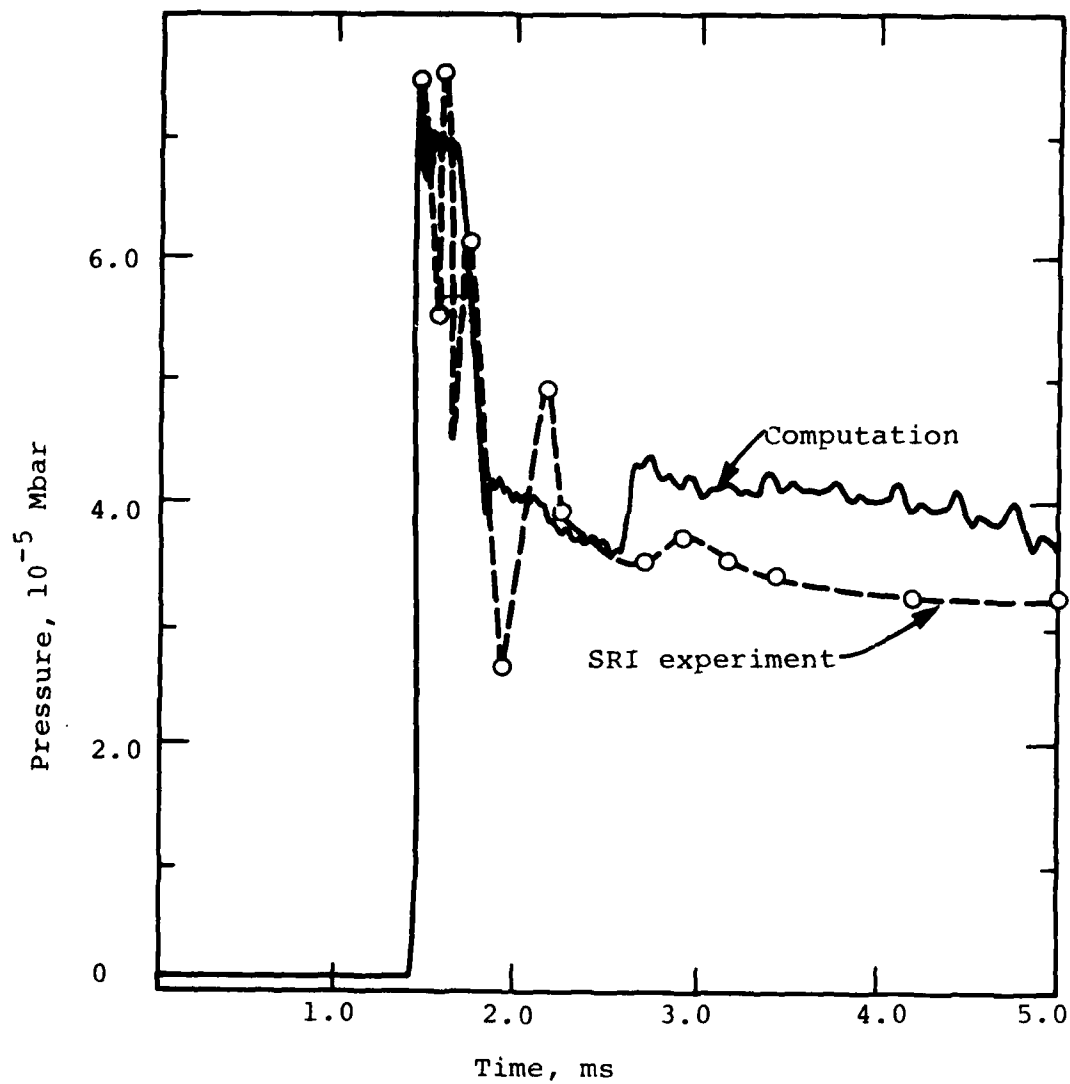
Figure 8   Comparison of computed and measured pressure
            histories at the reflecting wall, SRI Test 11
            (no venting).

Figures 9 and 10 show the computed pressure-time histories
for locations 4 inches and 8 inches upstream from the reflecting
wall, respectively.   There were no gages at these locations.

Figure 11 depicts the computed roof velocity history at
4 selected locations.   The computed roof profile at various times
is shown in Figure 12.   Computed roof displacement histories at
the reflecting wall and the Pin 1 position (1-inch upstream from
the reflecting wall) are shown in Figures 13 and 14.   Figure 15
shows computed pressure profiles in the trench at various times.
The shock propagation and reflection as well as the movement of
the driver gas/air discontinuity can be examined by means of
these figures.   Figure 16 shows the computed arrival time versus
distance for the shock and the driver gas/air discontinuity.
Upon reflection the shock propagates through the driver gases
and decelerates.

79-5-59
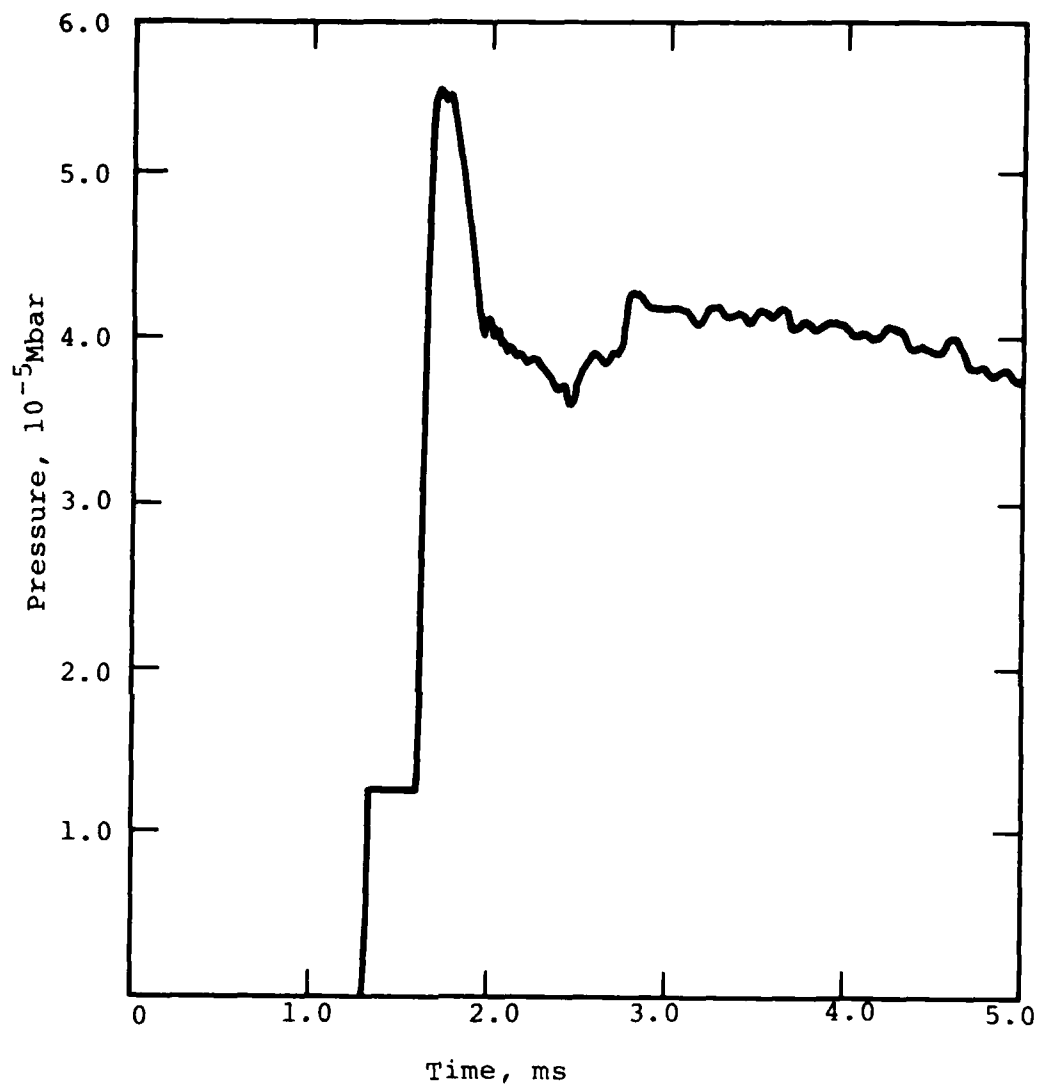
Figure 9   Computed pressure history at 4 inches from
the reflecting wall, SRI Test 11.

30

79-5-71
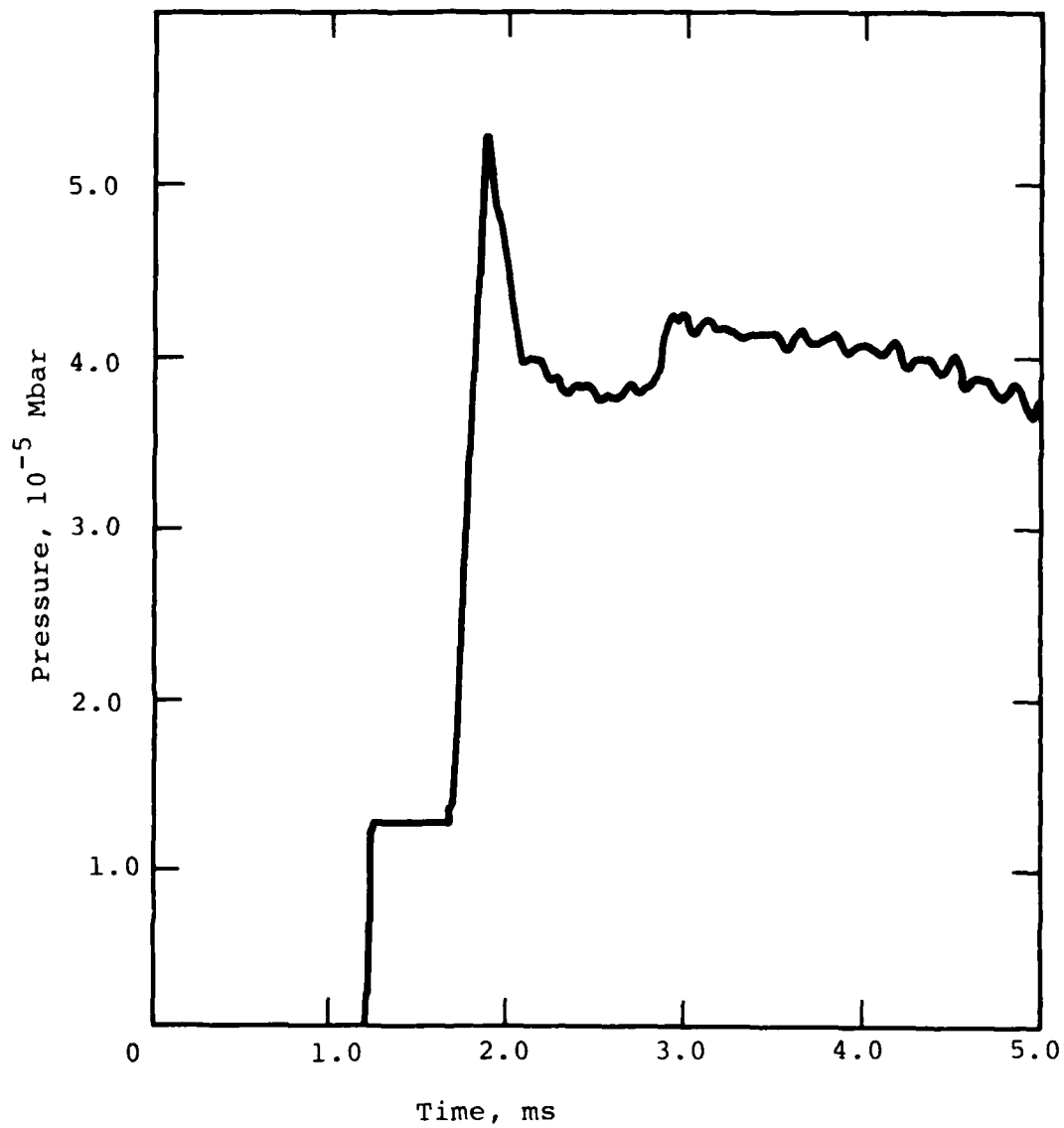
Figure 10   Computed pressure history at 8 inches from
             the reflecting wall, SRI Test 11.
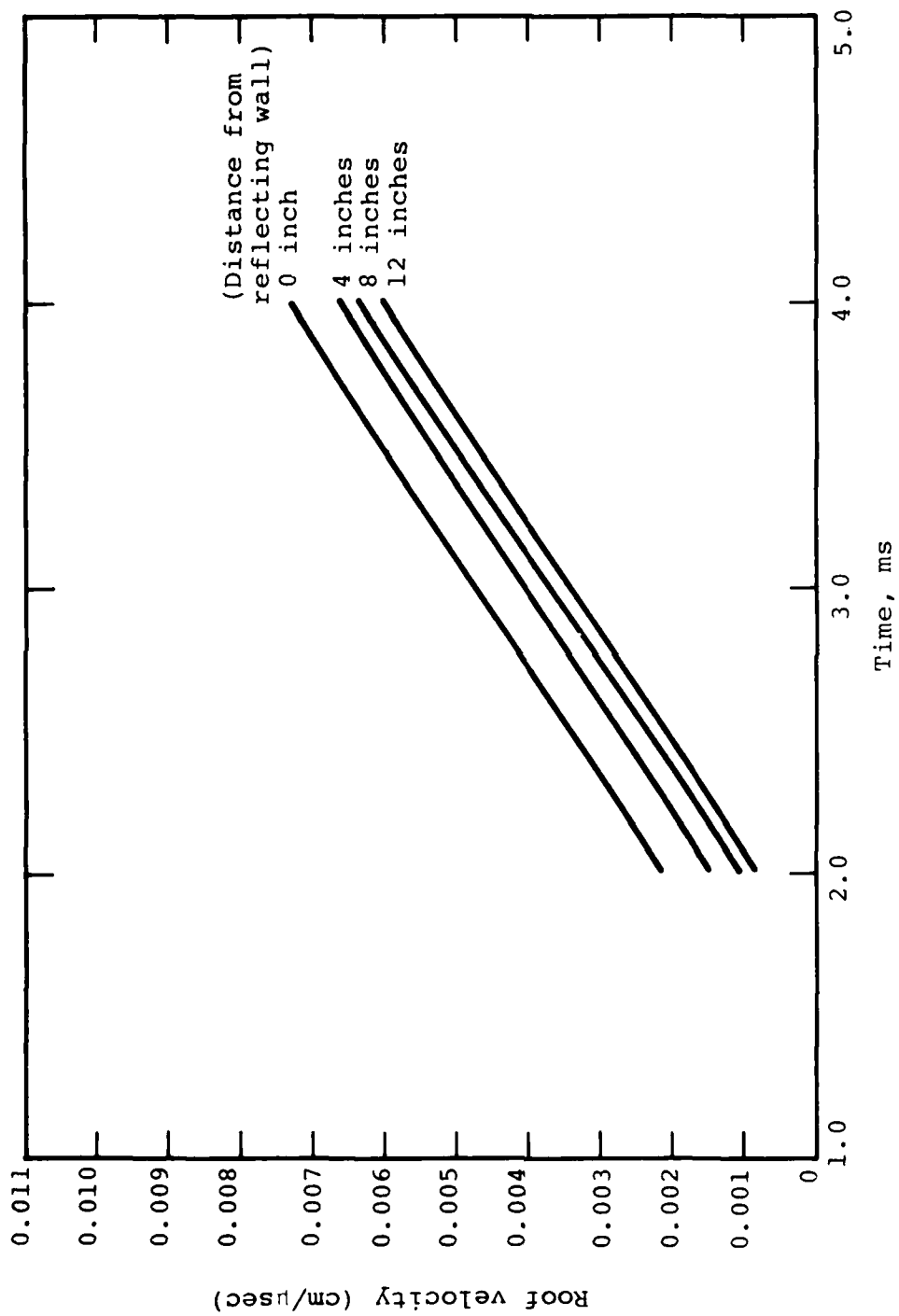
Figure 11 Computed roof velocity history at several locations in the trench, SRI Test 11.
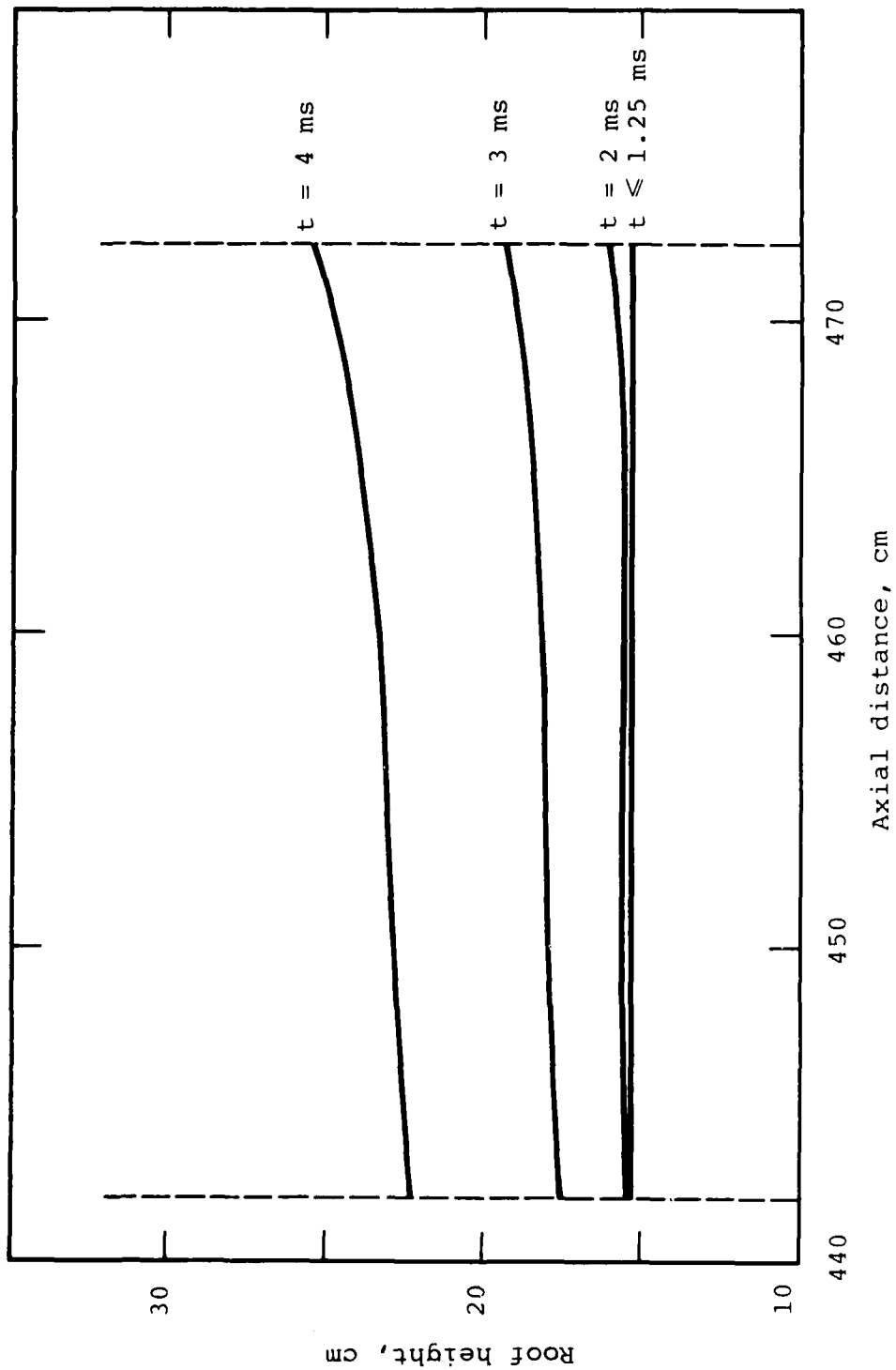
Figure 12   Computed roof profile at various times, SRI Test 11.

79-5-73

33

Figure 13   Computed roof displacement history at
              the reflecting wall, SRI Test 11.

Figure 14   Computed roof displacement history at Pin 1
location, SRI Test 11.

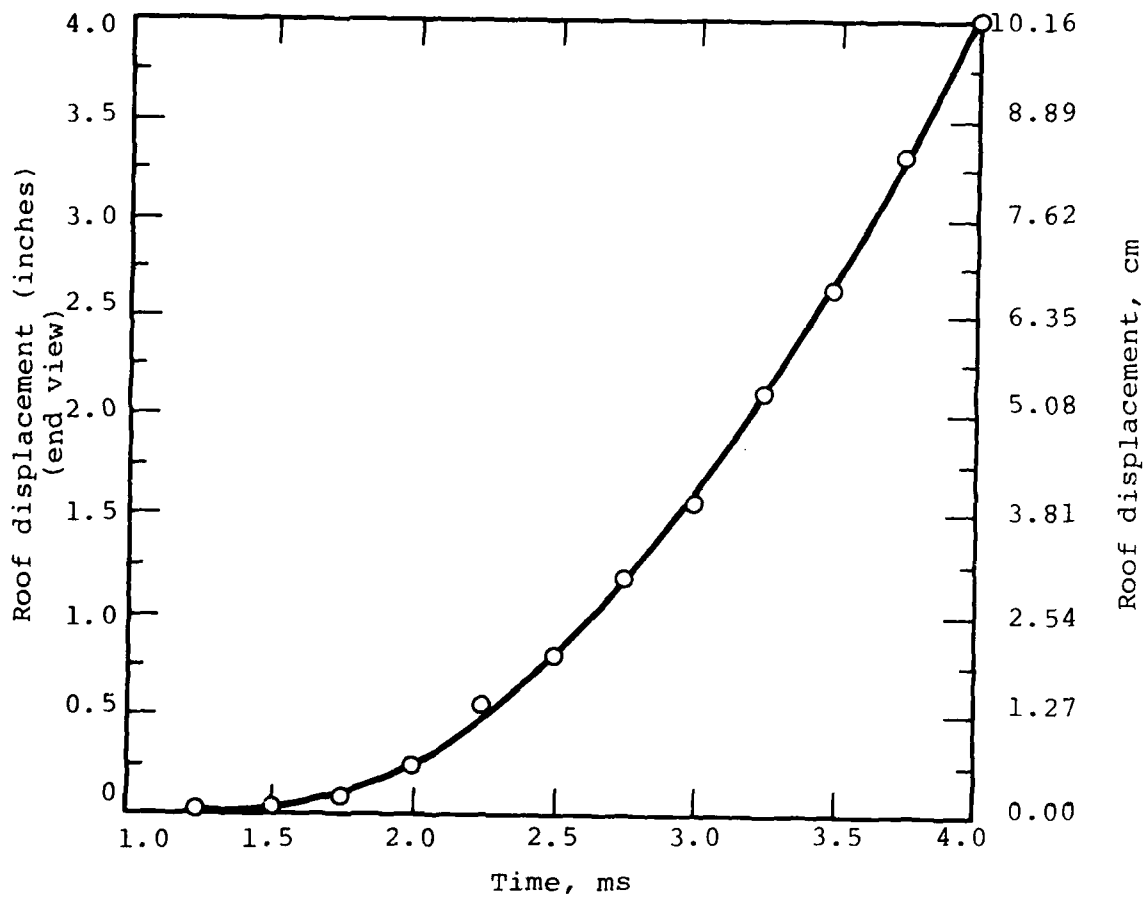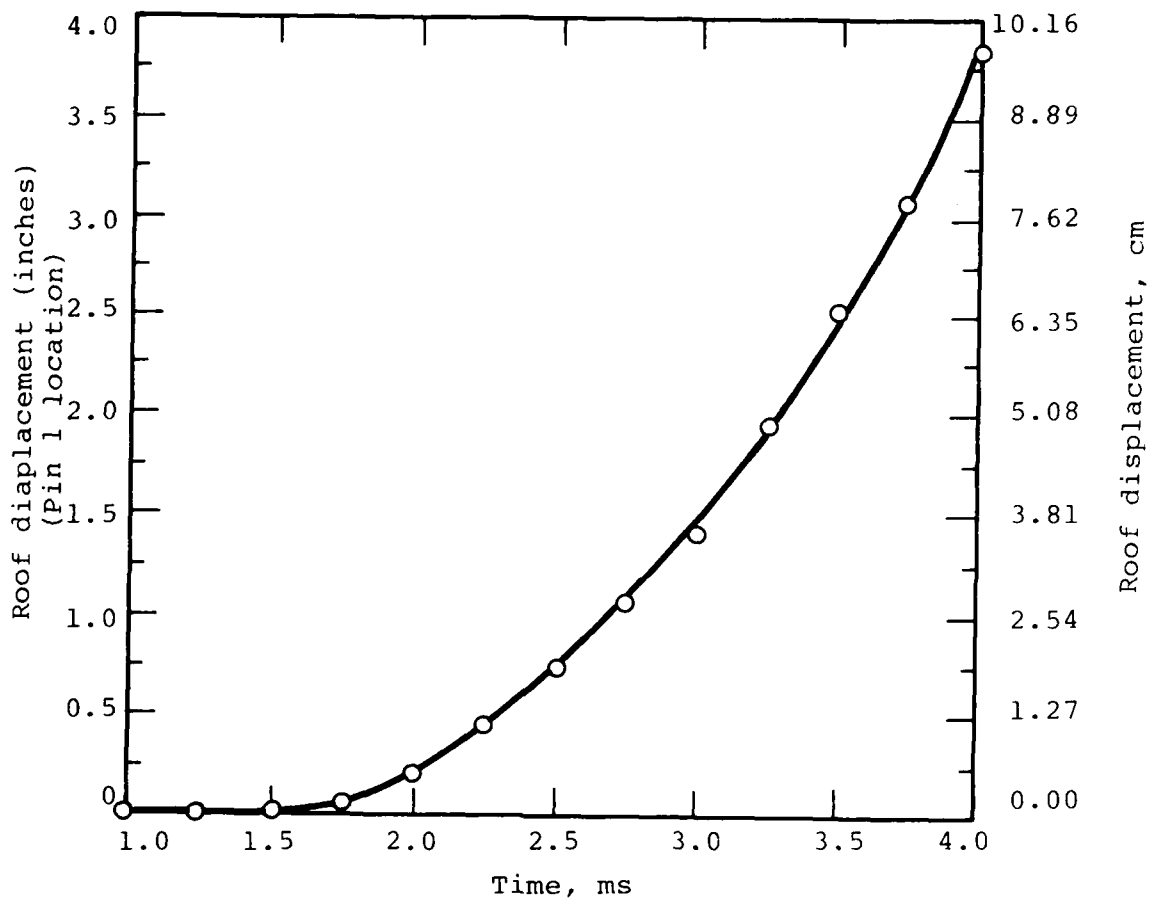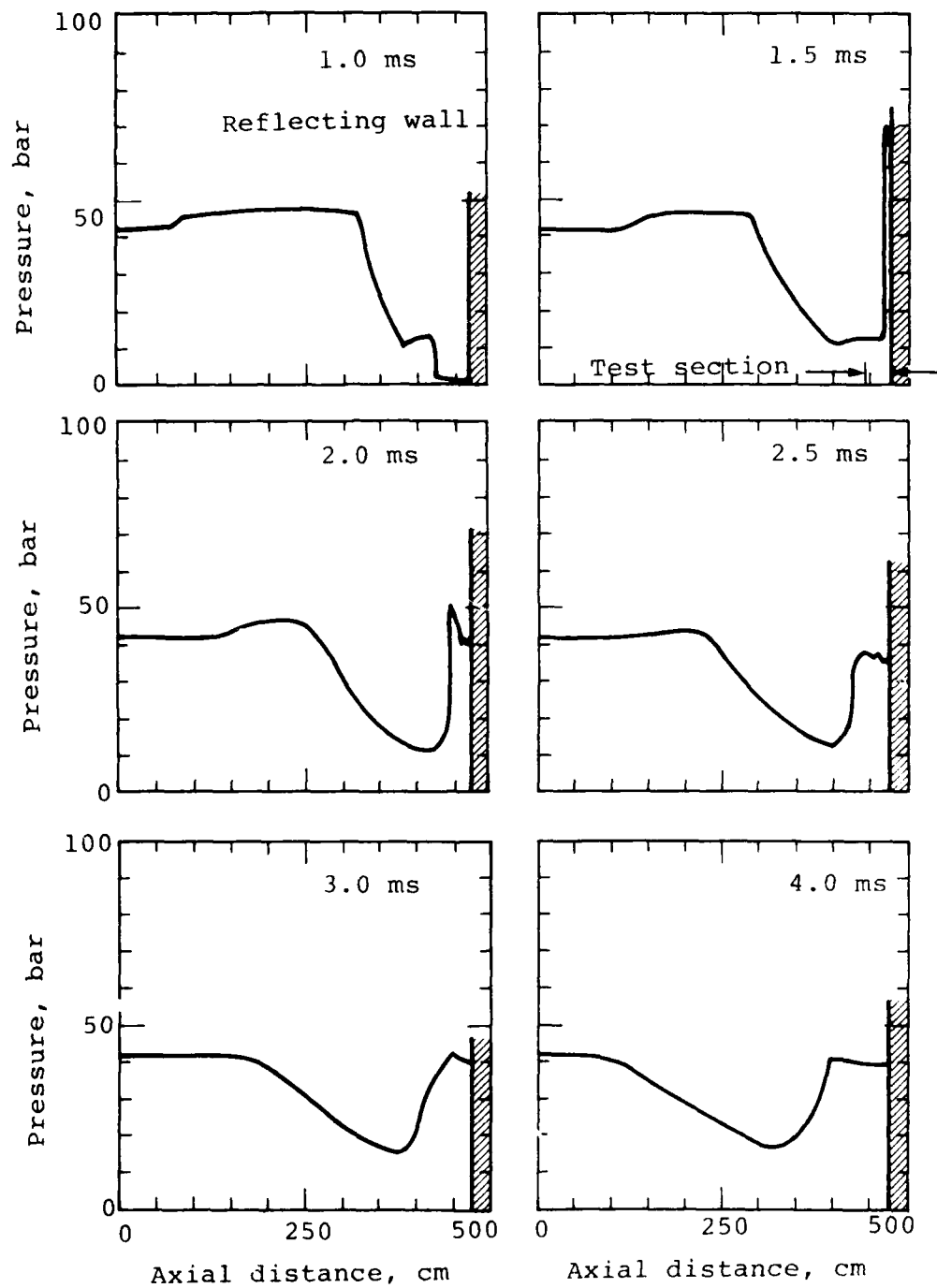Figure 15   Computed pressure profiles in the trench at
selected times, SRI Test 11.

79 5-77
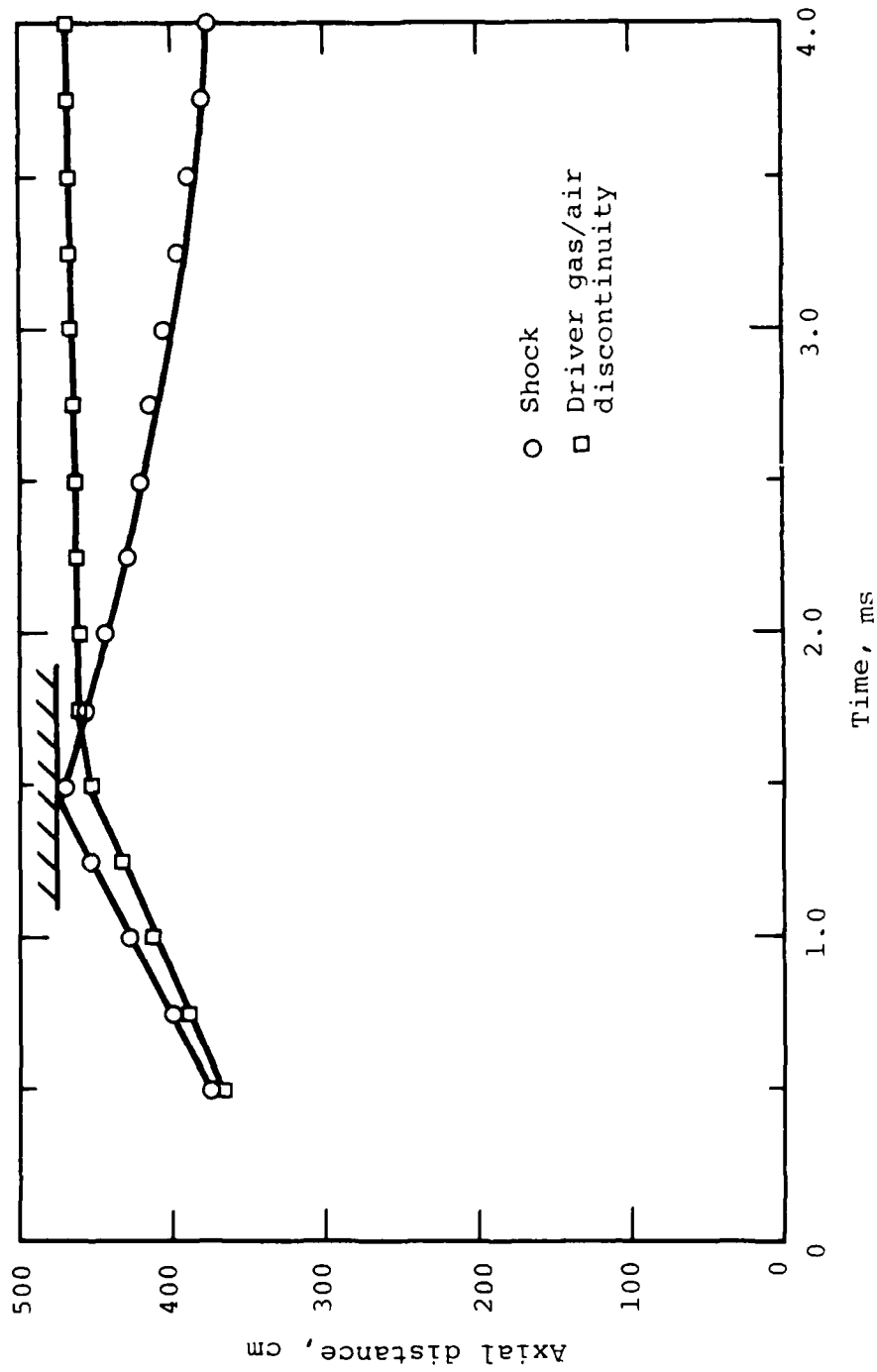
Figure 16 Location of shock front and contact discontinuity in the trench
as a function of time, SRI Test 11.

37

SECTION 4

COMPUTATIONAL RESULTS FOR TEST 17

The amount of primacord in the driver section of Test 17 was nominally identical to Test 11. In the calculation of Test 17, the driver and run-up sections were modeled the same as for Test 11, including the reduction of the initial internal energy density in the driver section to 0.75 of the nominal value, i.e., reduced to $E = 1.83 \times 10^{-4}$ Mbar-cc/cc.

In contrast to Test 11, the test section in Test 17 was a reinforced concrete pipe with a 3/4-inch wall thickness. As noted in Section 2.1, the concrete trench had two saw cuts, each offset from the crown by 55 degrees. The depth of the cuts was 0.9 of the wall thickness.

The high speed photography from the experiment (Reference 2) shows that the concrete trench fractured at a number of places. Two fractures occurred in the roof panel (i.e., between the saw cuts). The two fractures were about equally spaced from the crown (between 10 and 20 degrees). Gas jets formed through both of these "crown cracks" and both jets appeared to have penetrated to the surface. The venting model (see Section 2) was incorporated into the calculations of Test 17, although the model assumed only a single gas jet in the crown.

In SRI Test 17, gages were located at 38.5 and 15.5 inches upstream from the reflecting wall as well as at the reflecting

38

wall itself. Figure 17 compares the experimental and computed
pressure histories at the 38.5 inch gage location.* The theo-
retical and experimental pressures histories agree well at early
times. In the calculation, the reflected pressure pulse arrives
at this location at about 3 ms and pressure increases from about
15 bars to a maximum of about 38 bars at a time of about 4.1 ms.
The experimental data show a much lower amplitude reflected pulse
which arrives at about 4 ms. This discrepancy between the compu-
tational results and experimental data is not understood. Much
better agreement between the computation and experiment is
achieved at the other gage locations.

Figure 18 compares the measured and computed pressure
histories at the 15.5-inch gage location. The computed and
measured incident pulse amplitudes agree within 10 percent;
the computation having the higher incident pressure. Both the
experimental data and the computation show the reflected pulse
arriving at this location at about 2 ms with pressure increasing
to a maximum of about 40 bars. The computed and observed decay
of pressure following the peak agree well. Overall, the agree-
ment between the computed and measured pressure histories at
this location is considered good.

Figure 19 compares the computed and measured pressure
histories at the reflecting wall. There is good agreement
between the experimental data and the computational results in
terms of the overall shape and character of the pressure pulse
at this location. The computed and measured peak pressures agree
very well. There is also good agreement between the computed and

_____

*Note that in·Figures 17, 18, and 19 the times-of-arrivals
 of the measured and computed pressure histories have been
 forced to coincide (see Section 2).

39

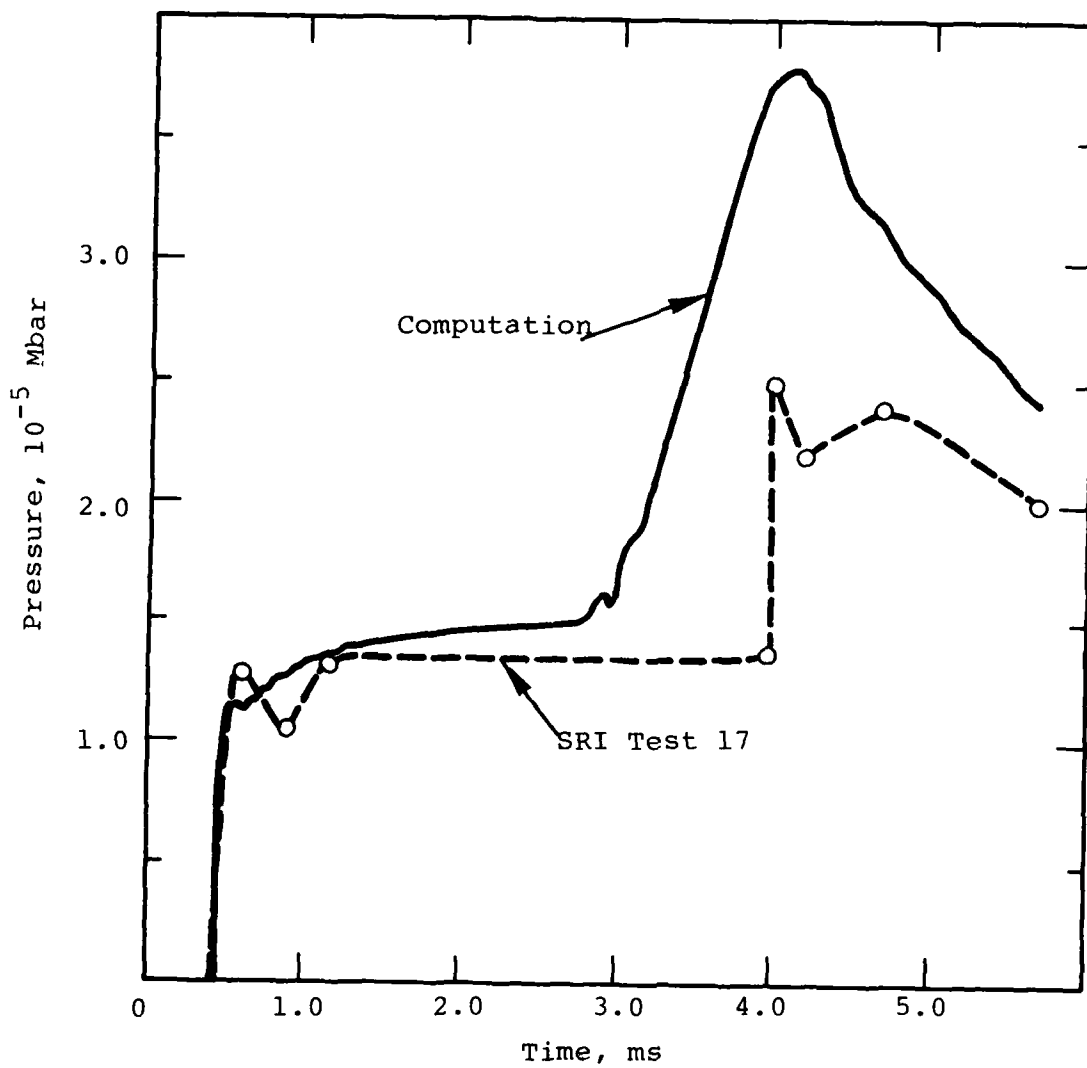Figure 17   Comparison of computed and measured pressure
            histories at 38.5 inches from the reflecting
            wall, SRI Test 17.
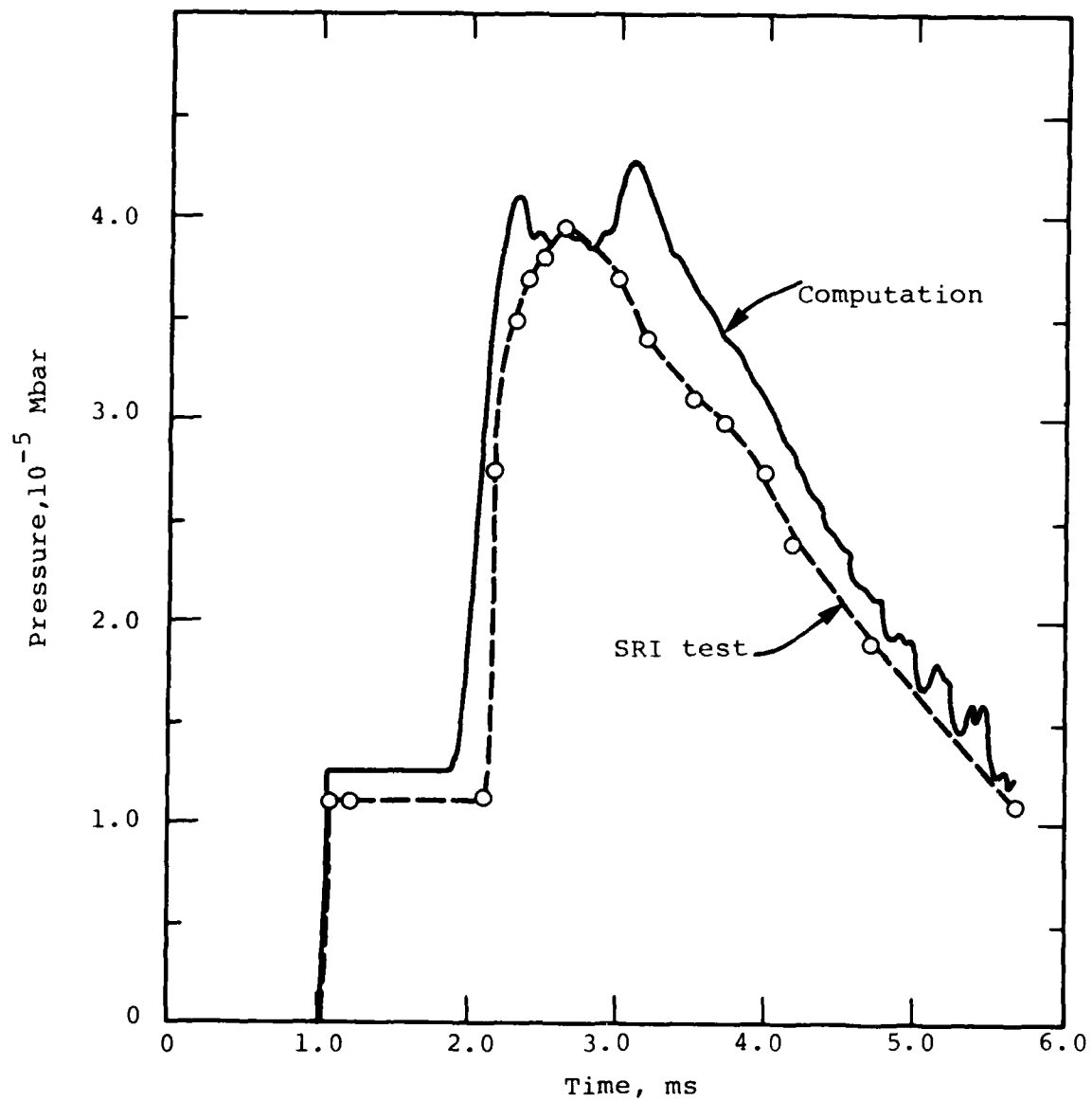
Figure 18   Comparison of computed and measured and pressure
            histories at 15.5 inches from the reflecting wall,
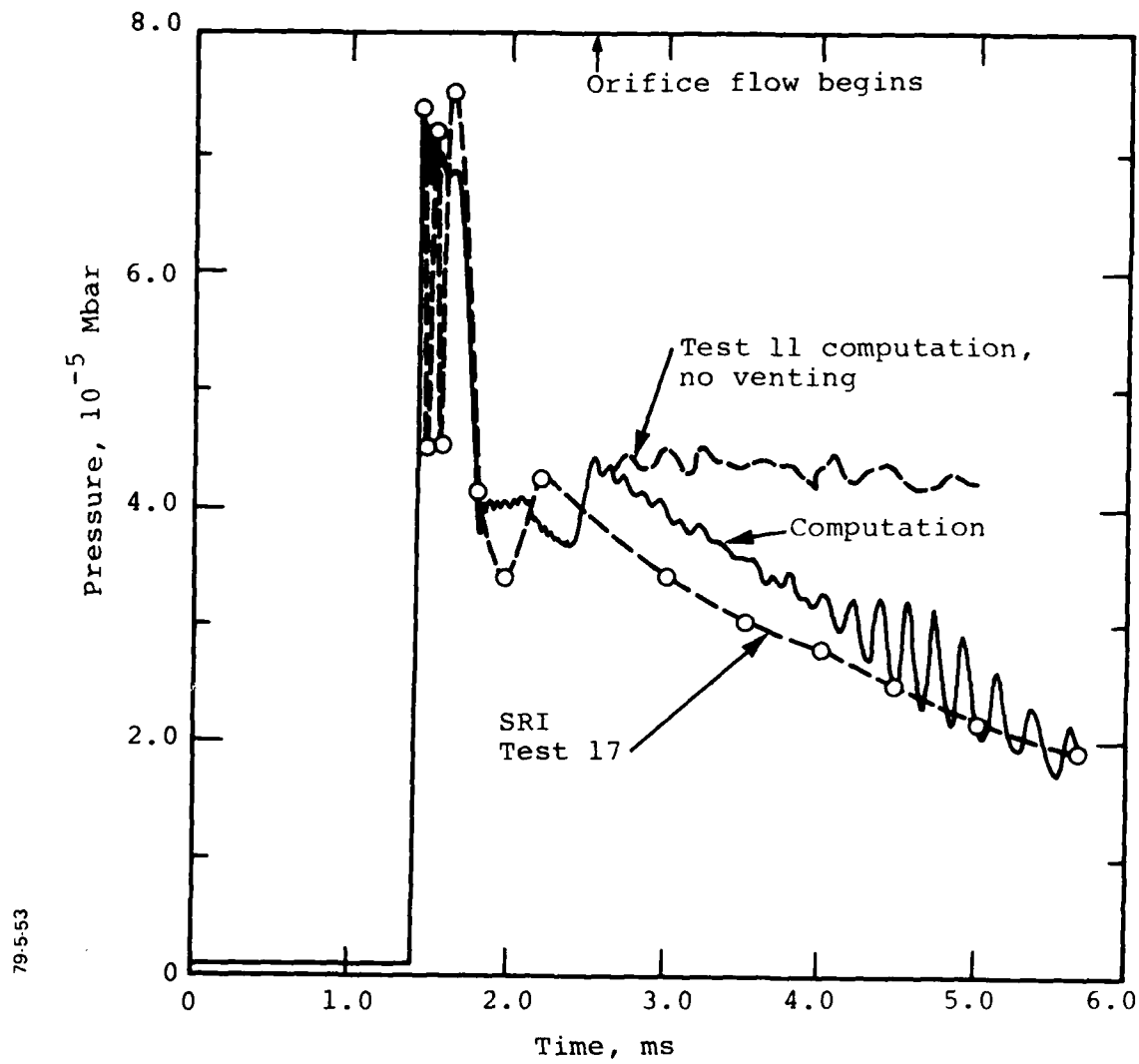   SRI Test 17.

Figure 19   Comparison of computed and measured pressure
             histories at the reflecting wall, SRI Test 17.

measured amplitude for the secondary peak occurring between 2 and 2.5 ms, although there is a small difference between the computed and measured times when this secondary peak occurs. The Test 11 computed pressure at the same location is also plotted, showing the effect of venting on the in-trench pressure.

At late times, following the secondary peak, the measured pressures are slightly lower than those computed. However, there is good agreement between the computational results and the experimental data in terms of the rate of attenuation of pressure with time following the secondary peak.

Although the computed and observed late-time rates of attenuation of pressure are in good agreement, it is not certain that the physical cause of this attenuation is the same for both. In the calculation, the attenuation of the in-trench pressure at late times is controlled by venting. Jet penetration begins at the time of shock arrival at the reflecting wall ($\sim$1.3 ms) and the jet penetrates the overburden and orifice flow begins about 1.1 ms later. From the Test 17 HYCAM photography, jet penetration of the overburden and venting to the atmosphere appears to begin about 2.4 ms after shock arrival at the reflecting wall. Examination of the Test 17 pressure histories (Reference 1) reveals no obvious change in the rate of attenuation of pressure with time at 2.4 ms after shock arrival.

Recalling that Tests 11 and 17 were nearly identical except that Test 11 showed no venting, comparison of the measured pressure histories at the reflecting wall (Figure 19) reveals a distinct difference in the rate of attenuation of pressure with time between the two experiments beginning about 1.5 ms after shock arrival. If the difference in the late-time attenuation of pressure with time between these two experiments is not the result of some venting mechanism, its cause is not clear.

In summary, although the computed and measured pressure histories at the reflecting wall for Test 17 are in very good overall agreement, the agreement in terms of the late-time attenuation of the in-trench pressure may be fortuitous and cannot be interpreted as supporting the venting model used in the calculation.

Figures 20 and 21 are the computed pressure histories at locations 4 and 8 inches upstream from the reflecting wall, repectively. Recalling that Tests 11 and 17 were nearly identical except that Test 11 showed no venting, comparisons of Figures 20 and 21 with Figures 9 and 10, illustrate the effect of venting on the computed late-time trench pressure. The effect of venting on the late-time pressure in the trench is discussed in somewhat more detail in Section 5.

Figure 22 shows the computed roof velocity history for four selected points in the test section. Figure 23 shows the computed roof profile at selected times.

Figure 24 compares the computed and observed displacement of the trench "roof" at the reflecting wall. The computed displacements are slightly higher than observed, and tend to diverge from the test data at late times. This divergence of the computed displacements from the observations has two causes. First, and most important, the computed late-time pressure in the trench was slightly higher than measured (see Figure 19). Second, for times greater than about 3.2 ms, the trench "walls" and "floor" were not permitted to move in the calculation and thus for later times all expansion of the trench cross-sectional area is achieved by upward displacement of the roof. In reality of course, even though the trench expands preferentially upward at

44
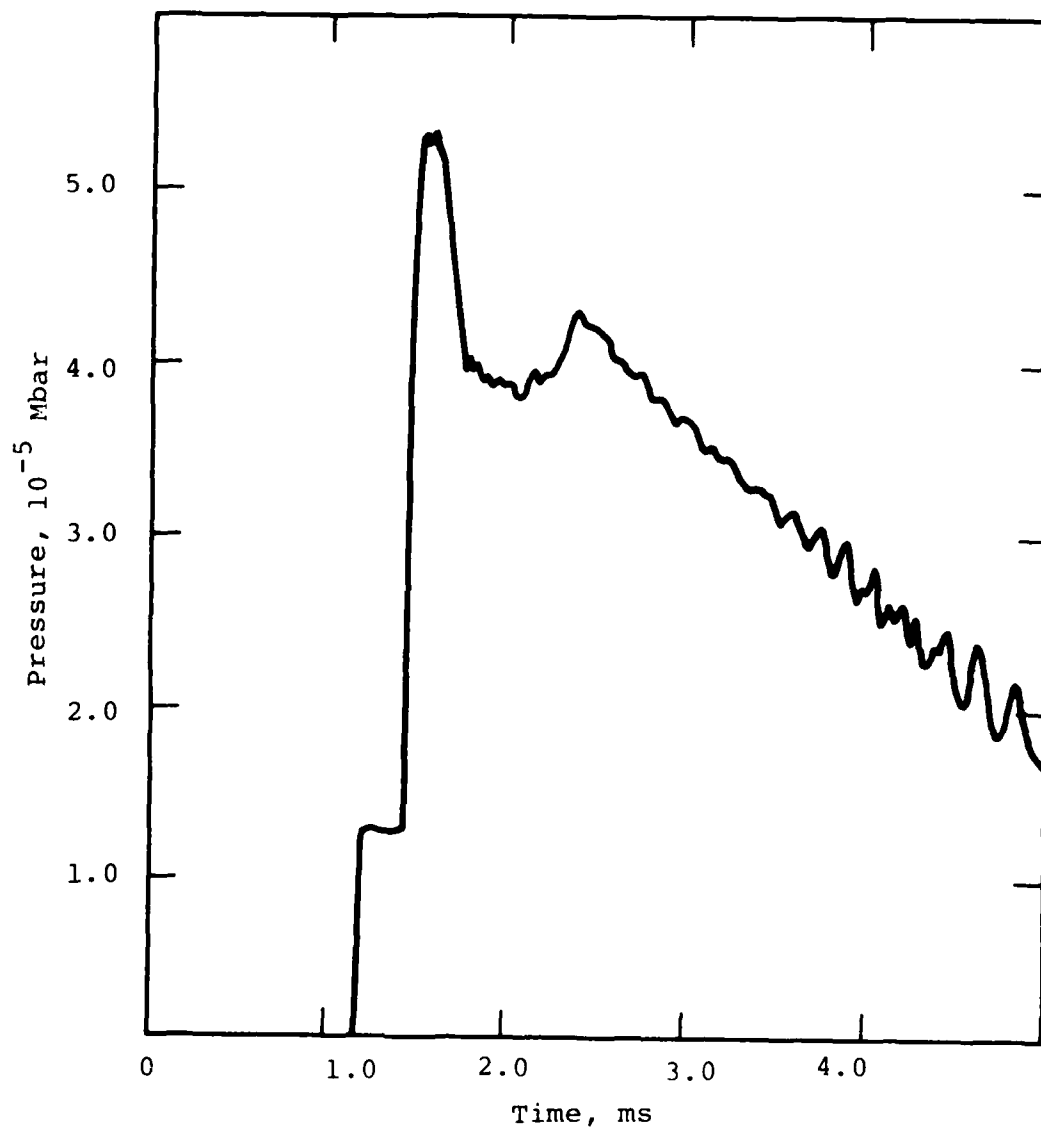
Figure 20   Computed pressure history at 4 inches from
the reflecting wall, SRI Test 17.
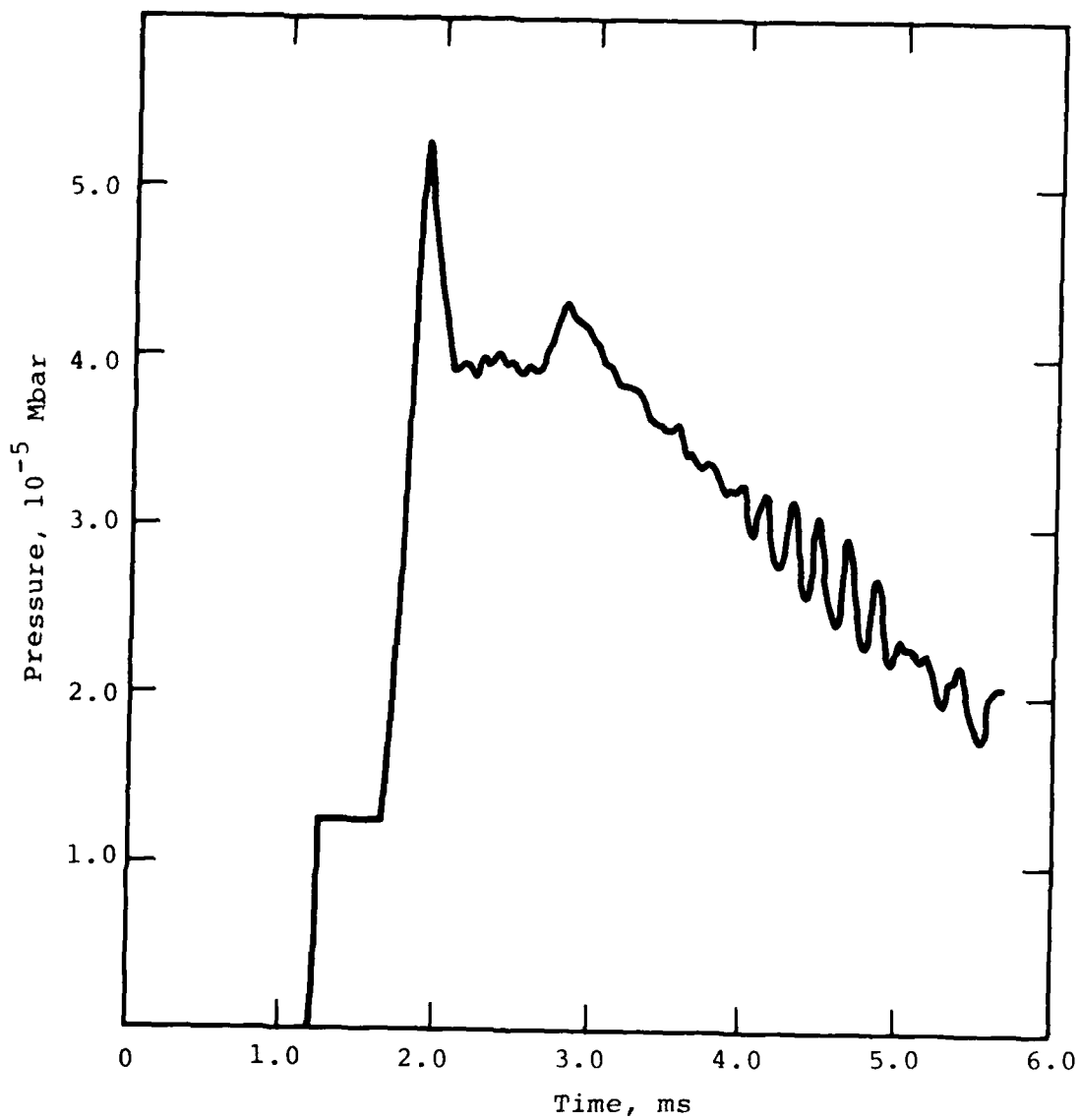
Figure 21   Computed pressure history at 8 inches from
             the reflecting wall, SRI Test 17.
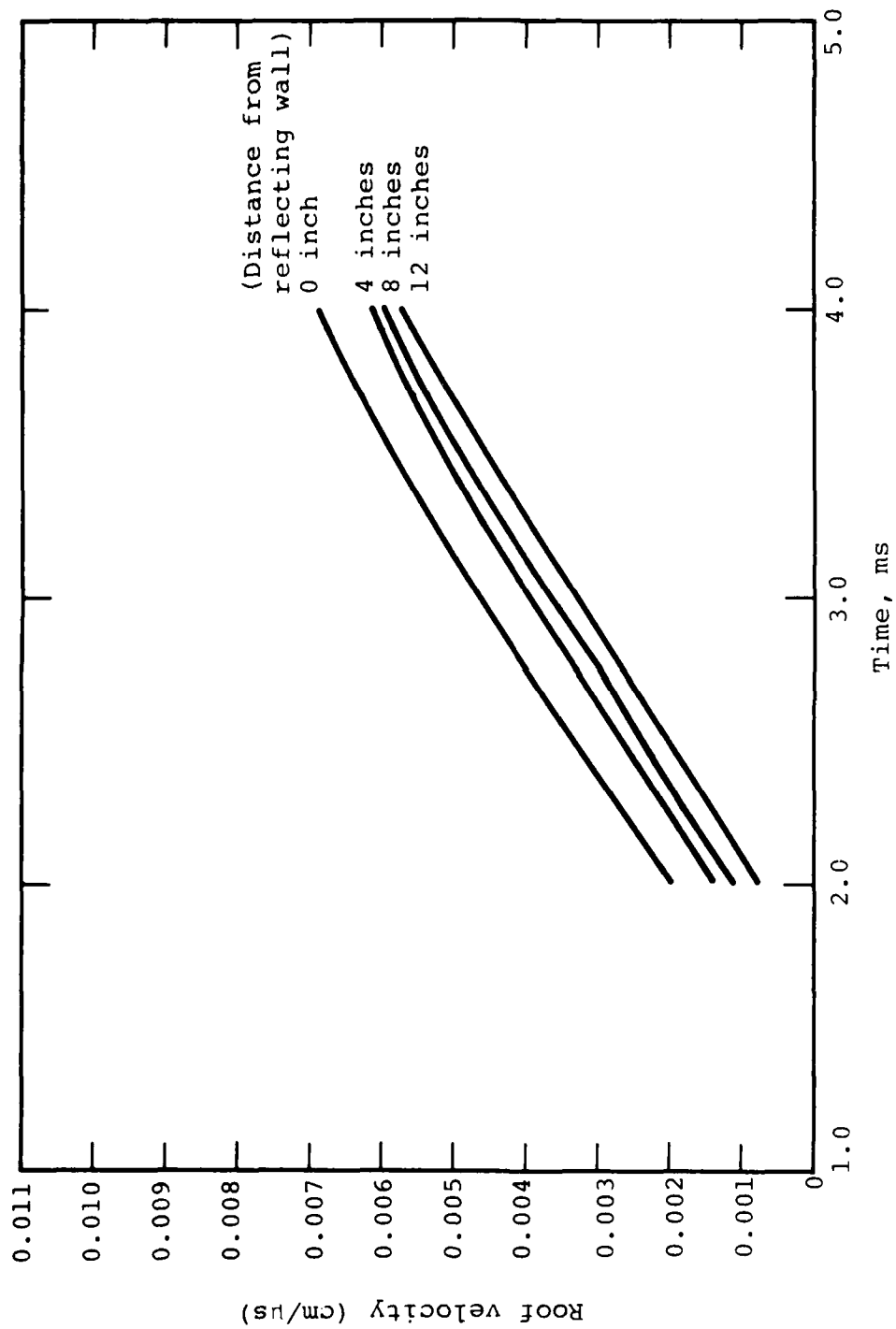
Figure 22   Computed roof velocity history at several locations in the trench, SRI Test 17.
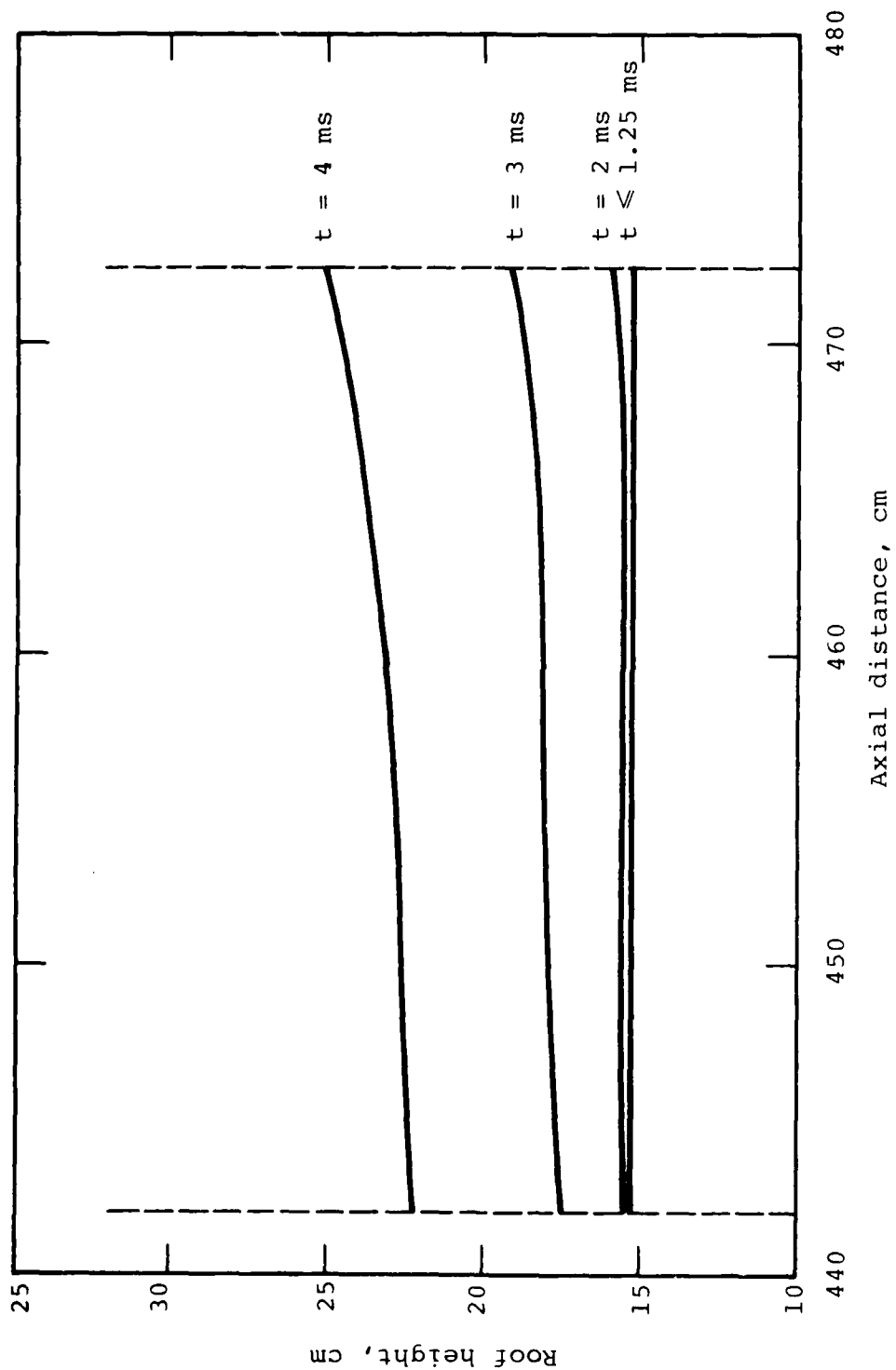
Figure 23   Computed roof profiles at various times, SRI Test 17.
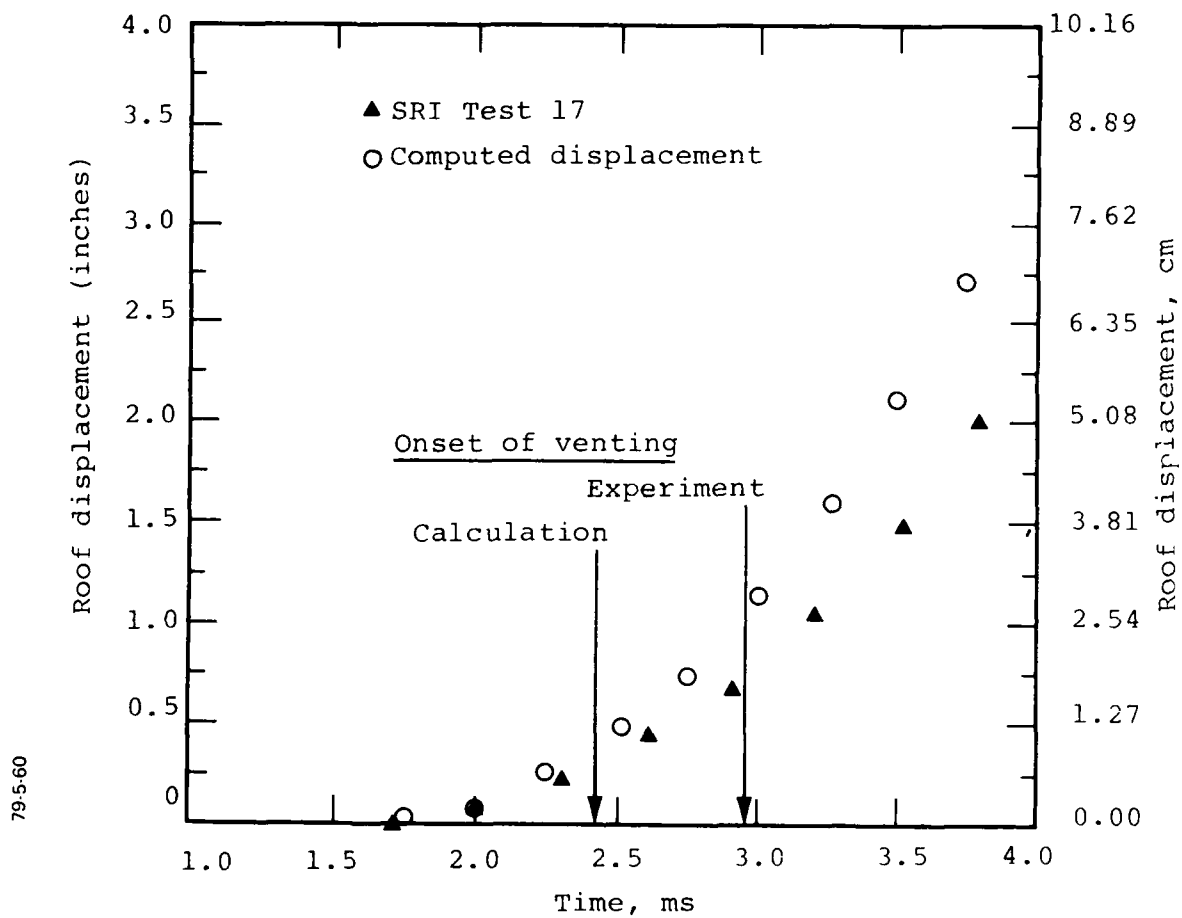
Figure 24   Comparison of computed and measured roof
             displacement history at the reflecting
             wall, SRI Test 17.

late times, some expansion of the "walls" and "floor" continues. This may be seen in Figure 25 which compares the computed and experimentally observed displacement of the trench "wall" versus time.

Figure 26 shows the computed pressure profiles in the trench at selected times. Comparison of this figure with Figure 15 also illustrates the effect of venting of the computed late-time pressures in the trench.

Figure 25   Comparison of computed and measured wall
             displacement history at the reflecting
             wall, SRI Test 17.

51

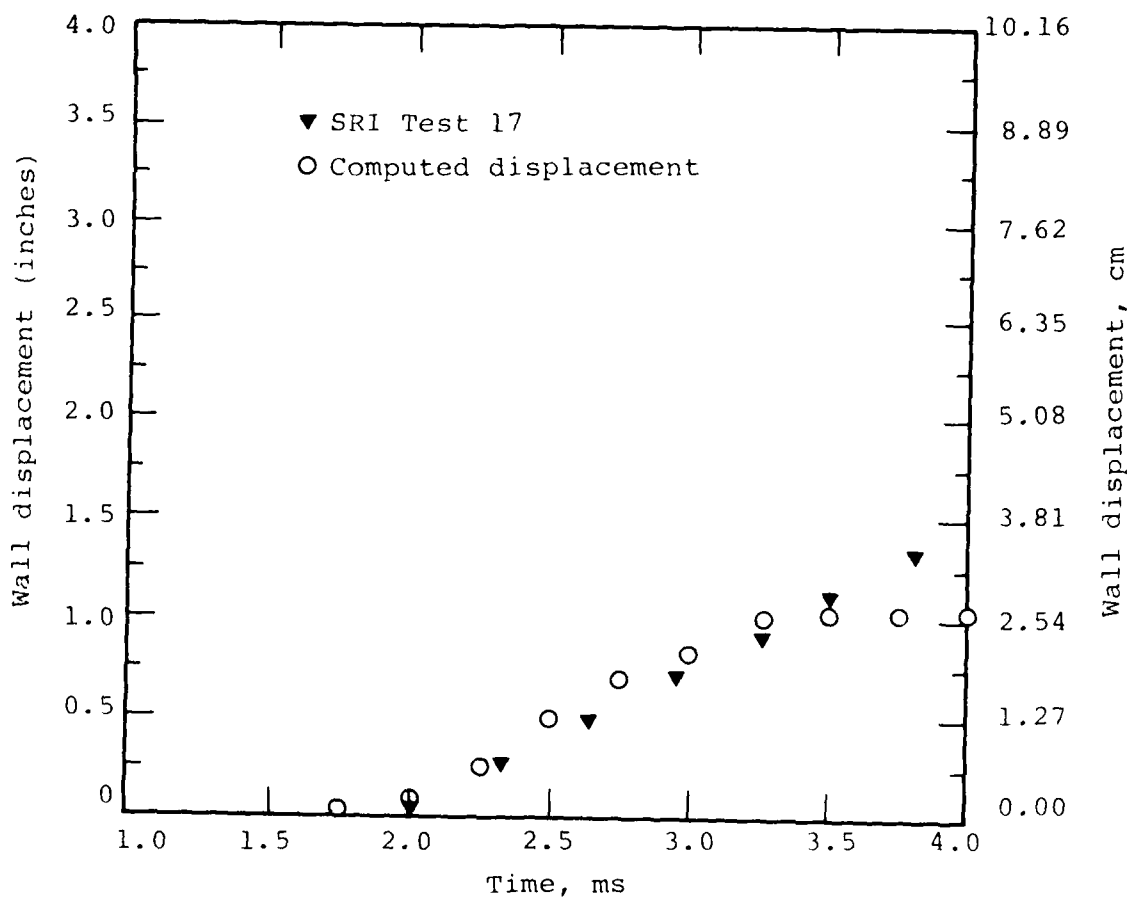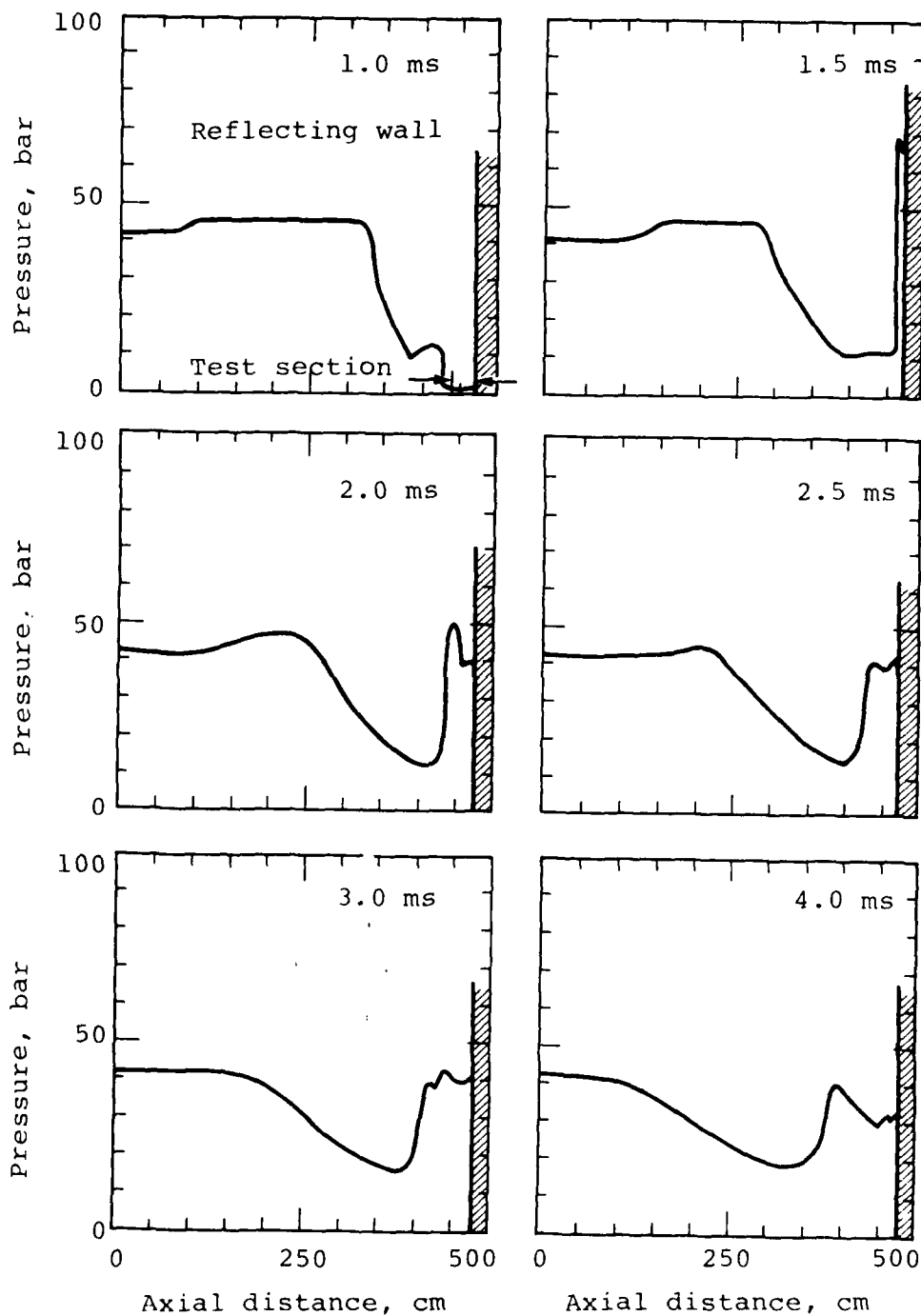Figure 26   Computed pressure profiles in the trench at various times, SRI Test 17.

SECTION 5

COMPUTATIONAL RESULTS FOR TEST 18

The amount of PETN used in the driver for Test 18 was twice that for Test 17 and the peak pressure at the reflecting wall for Test 18 was about twice that for Test 17. In Test 18, at total of 88 feet of 100 grain/ft Primacord was used in the driver section corresponding to a nominal initial density of 0.0141 g/cc and an initial energy density of 4.88×10^{-4} Mbar-cc/cc. However, to achieve in the calculation the observed amplitude for the incident pressure pulse in the run-up section, it was required to reduce the initial energy density in the driver section to 0.6 of the nominal value (i.e., $E = 2.928 \times 10^{-4}$ Mbar-cc/cc).

HYCAM photography (Reference 2) showed that the trench fractured in a number of locations. The trench roof panel fractured at the crown and the gas jet through this crown crack penetrated the soil overburden and vented to the atmosphere. thus the venting model was incorporated into the calculation.

Figure 27 compares the measured and computed pressure histories for the 38.5-inch gage location (in the run-up section) for Test 18. The agreement between the computed and measured pressure pulses at early times is reasonably good, considering the experimental trace is highly oscillatory. At a time of about 3 ms, the calculation shows the arrival of the reflected pressure pulse at this location and a consequent increase in pressure. In contrast, the
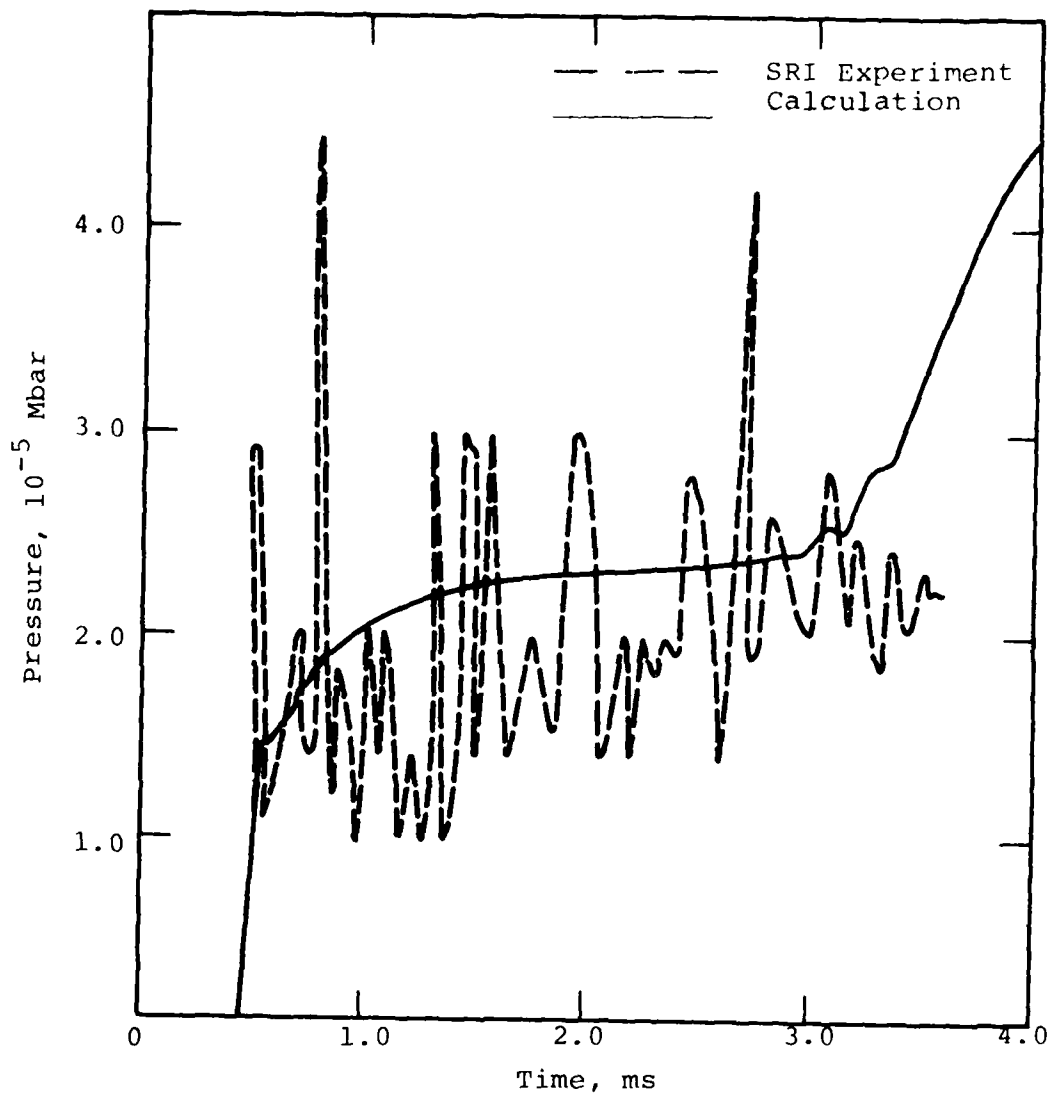
79-5-86

Figure 27   Comparison of computed and measured pressure histories
at 38.5 inches from the reflecting wall, SRI Test 18.

54

experimental data show the reflected pulse arriving at this loca-
tion at a time of about 4.7 to 5 ms. The measured peak pressure
of the reflected pulse is about 35 bars, which is lower than ob-
tained in the calculations. This discrepancy between the computed
and observed pressure waveform at this location is similar to
that noted for Test 17. Much better agreement between the calcu-
lated and measured pressure histories is achieved at the other
gage locations. The cause of the differences between the computed
and measured pressure histories in the run-up section at late
times, particularly in terms of the time-of-arrival and amplitude
of the reflected pressure pulse, is not known.

Figure 28 compares the computed and measured pressure his-
tories for the 15.5-inch location. The results of two computations
are shown, one incorporating the venting model described in
Section 2, and one without venting. The measured and computed
amplitudes for the incident pulse at this location are virtually
identical. The computations show the reflected pulse arriving
at a time of about 1.75 ms with the maximum reflected pressure
of about 63 bars occurring at about 3 ms. The measured peak
reflected pressure is also about 63 bars but occurs at a time
of about 2.75 ms, slightly earlier than computed. The measured
risetime for the reflected pulse is faster than that computed.

At the 15.5 inch location, the decay of the pressure follow-
ing the maximum associated with the reflected pulse is controlled
by venting in the test section. The late-time pressure decay
for the calculation incorporating the venting model agrees very
well with the experimental data. On the other hand, for the
calculation in which no venting was allowed, the decay of the
trench pressure at late times is much slower than observed, and
at a time of 4 ms the computed trench pressure for the no-venting
case is nearly a factor of two higher than measured.
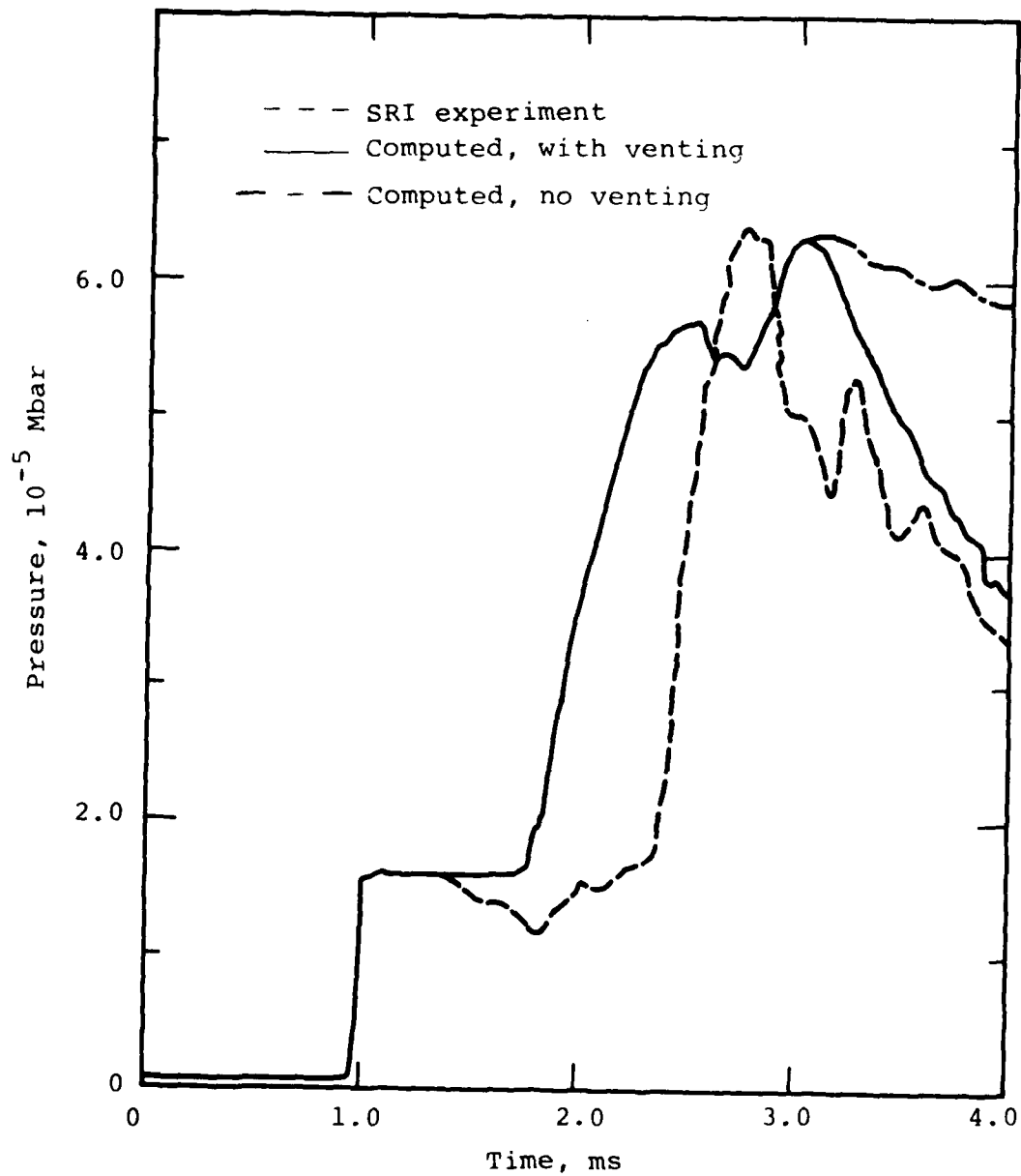
Figure 28   Comparison of computed and measured pressure
             histories at 15.5 inches from the reflecting
             wall, SRI Test 18.

56

Figure 29 compares the computed and measured pressure histories at the reflecting wall. Again, the results of two calculations are shown, one with and one without venting. The agreement between the early-time portions of the observed and computed pressure histories is very good. The peak pressures agree to within about 10 percent. Both the computed and measured pressure histories contain a secondary maximum following the initial peak although the measured amplitude of this recompression is significantly greater than the computed.

In the computation which incorporated the venting model, jetting at the reflecting wall began at the time of shock arrival and orifice flow from this portion of the trench began at a time of about 2.4 ms. That is, the jet required about 1.1 ms to penetrate the overburden in the calculation. This computed jet penetration time compared very favorably with the approximate 1.2 ms penetration time observed in the experiment (Reference 1).

The character of the computed pressure history at late times is controlled by the venting process. This is easily seen by comparing the late-time pressure histories for the venting and no-venting calculations as shown in Figure 29. The computed decay of pressure in the trench following venting closely approximates the experimentally observed attenuation. This agreement between the computed and measured pressure histories at late-times lends support to the venting model used in the calculation.

Figures 30 and 31 show the computed pressure histories for locations 4 inches and 8 inches upstream from the reflecting wall, respectively.
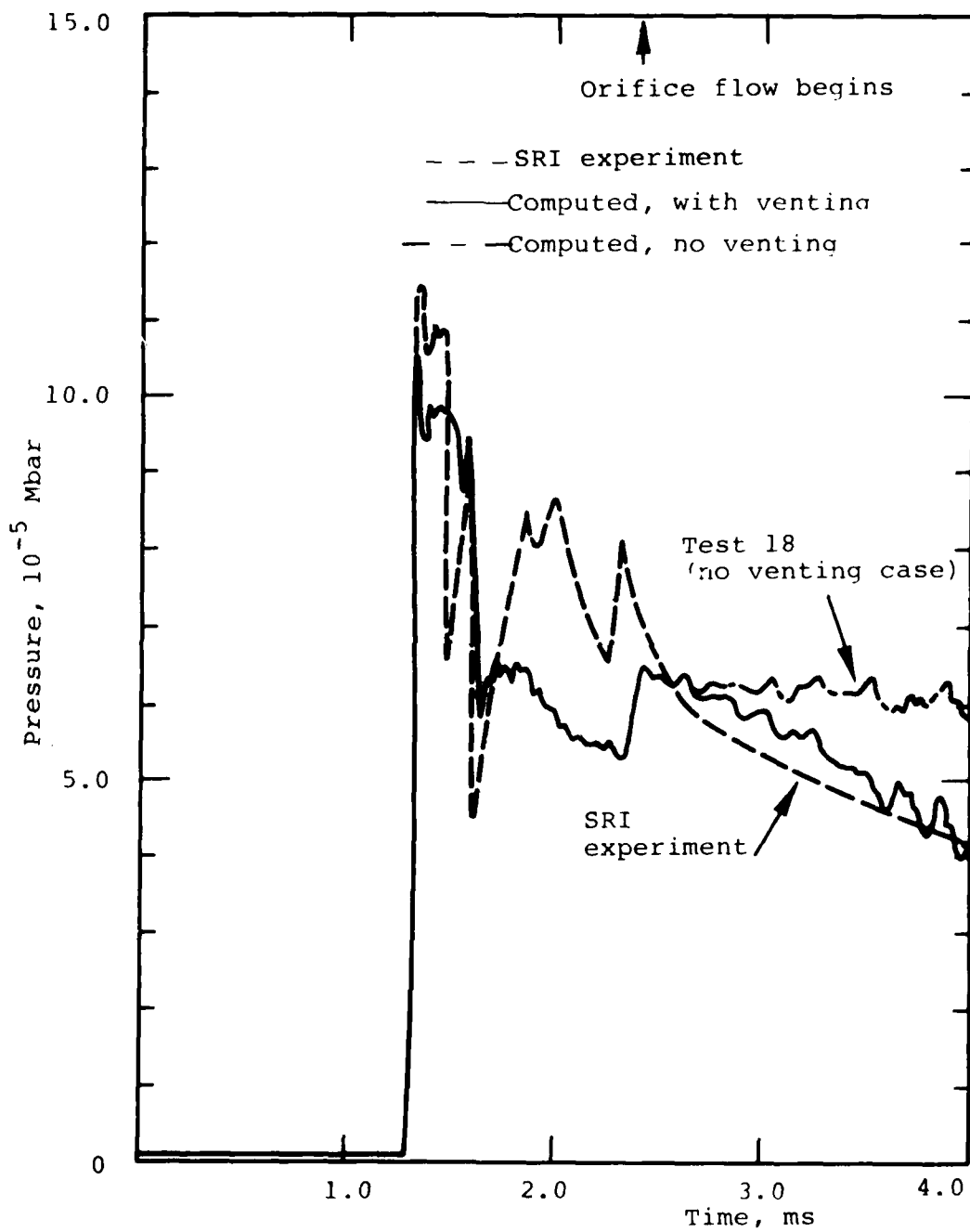
Figure 29   Comparison of computed and measured pressure
histories at the reflecting wall, SRI Test 18.
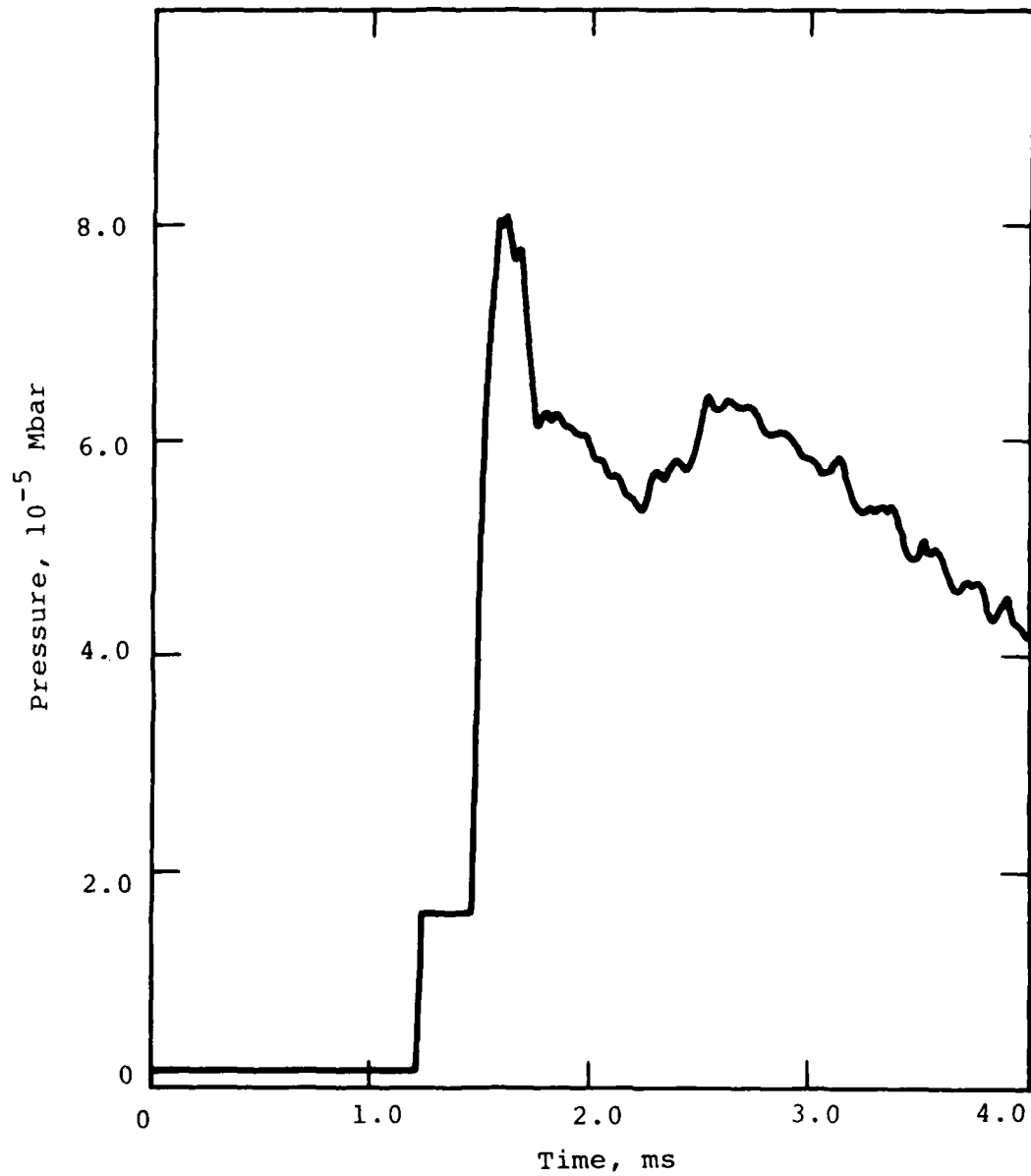
Figure 30   Computed pressure history at 4 inches from
the reflecting wall, SRI Test 18.
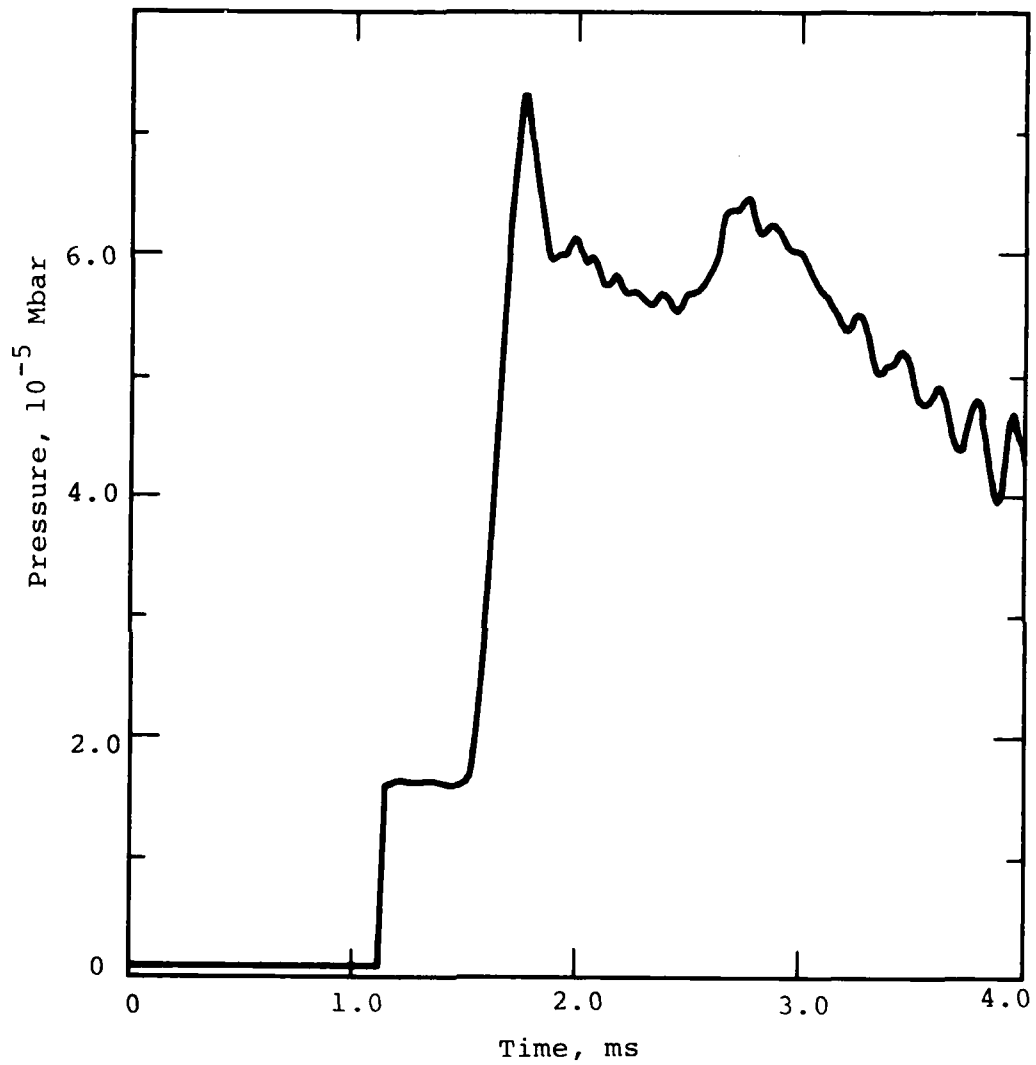
Figure 31   Computed pressure history at 8 inches from
the reflecting wall, SRI Test 18.

Figure 32 shows the computed "roof" velocities as a function of time for four specific locations in the test section.

Figure 33 shows the computed profile for the trench "roof" at times of 2 ms, 3 ms, and 4 ms.

Figure 34 compares the computed and observed displacement history of the trench roof at the reflecting wall. Figure 35 is a similar comparison for the Pin 1 position, one inch upstream from the reflecting wall. Figure 36 is a comparison of the computed and measured displacement history for the trench "wall." The theoretical results for the displacement of the trench roof and wall are in excellent agreement with the experimental data.

Figure 37 shows the computed pressure profiles in the driver, run-up and test sections at times of 1.0, 1.5, 2.0, 2.5, 3.0, and 4.0 ms. For times greater than 2.5 ms, the computed results from both the venting (solid) and no venting (dashed) cases are shown, illustrating the effect of venting on the in-trench pressure.
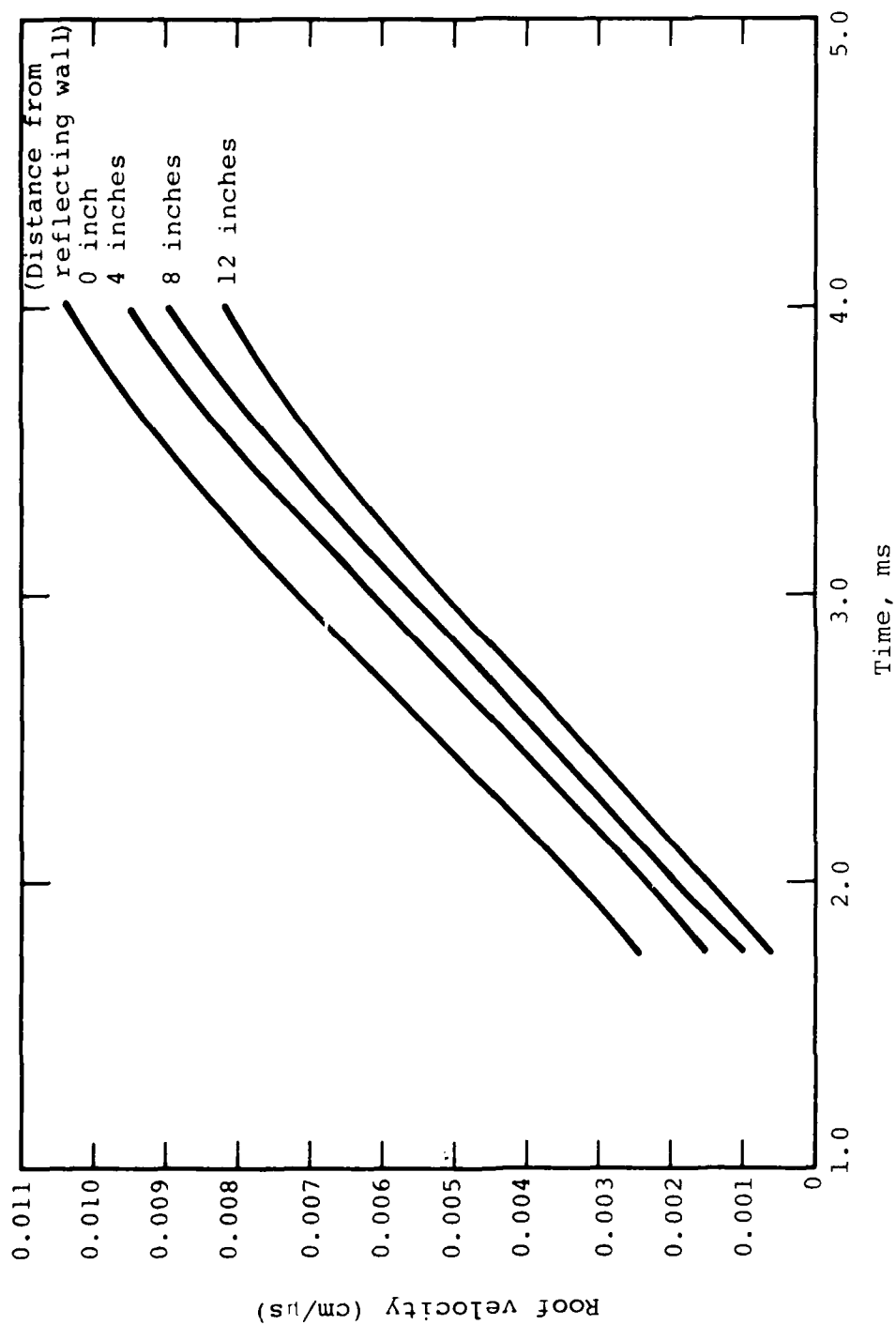
Figure 32   Computed roof velocity history at various locations in the trench, SRI Test 18.

79-5-91

62
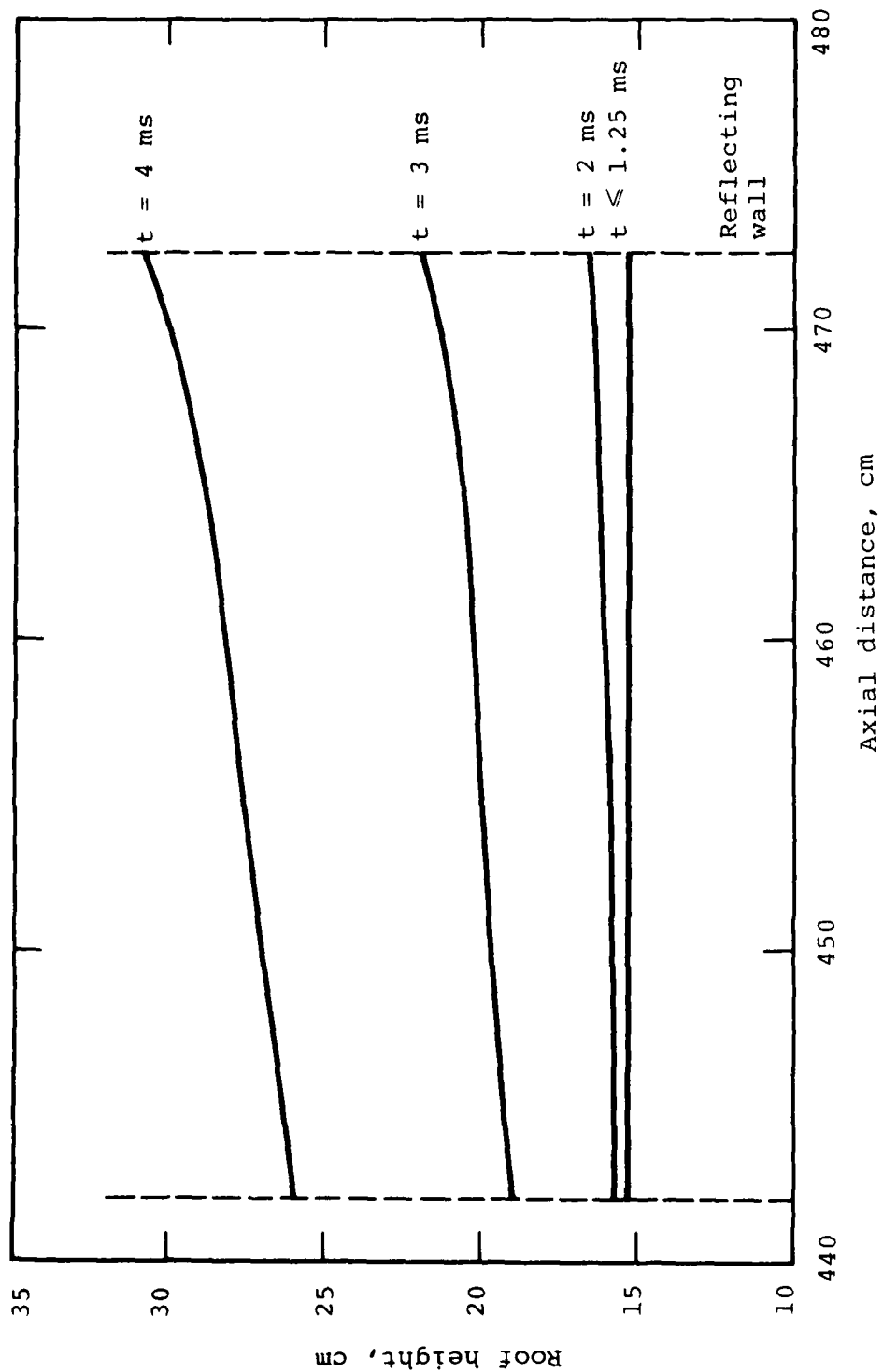
Figure 33   Computed roof profile at various times, SRI Test 18.

63
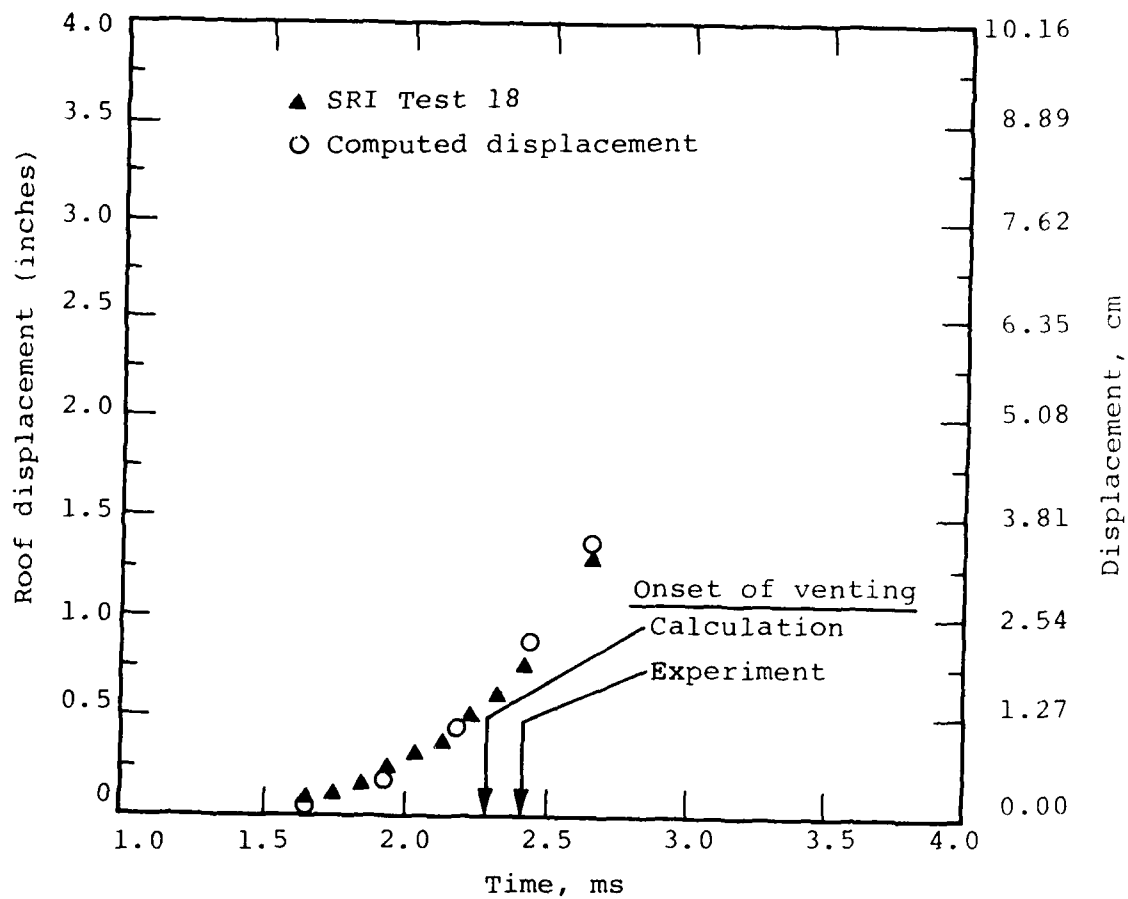
Figure 34   Comparison of computed and measured roof
displacement histories at the reflecting
wall, SRI Test 18.
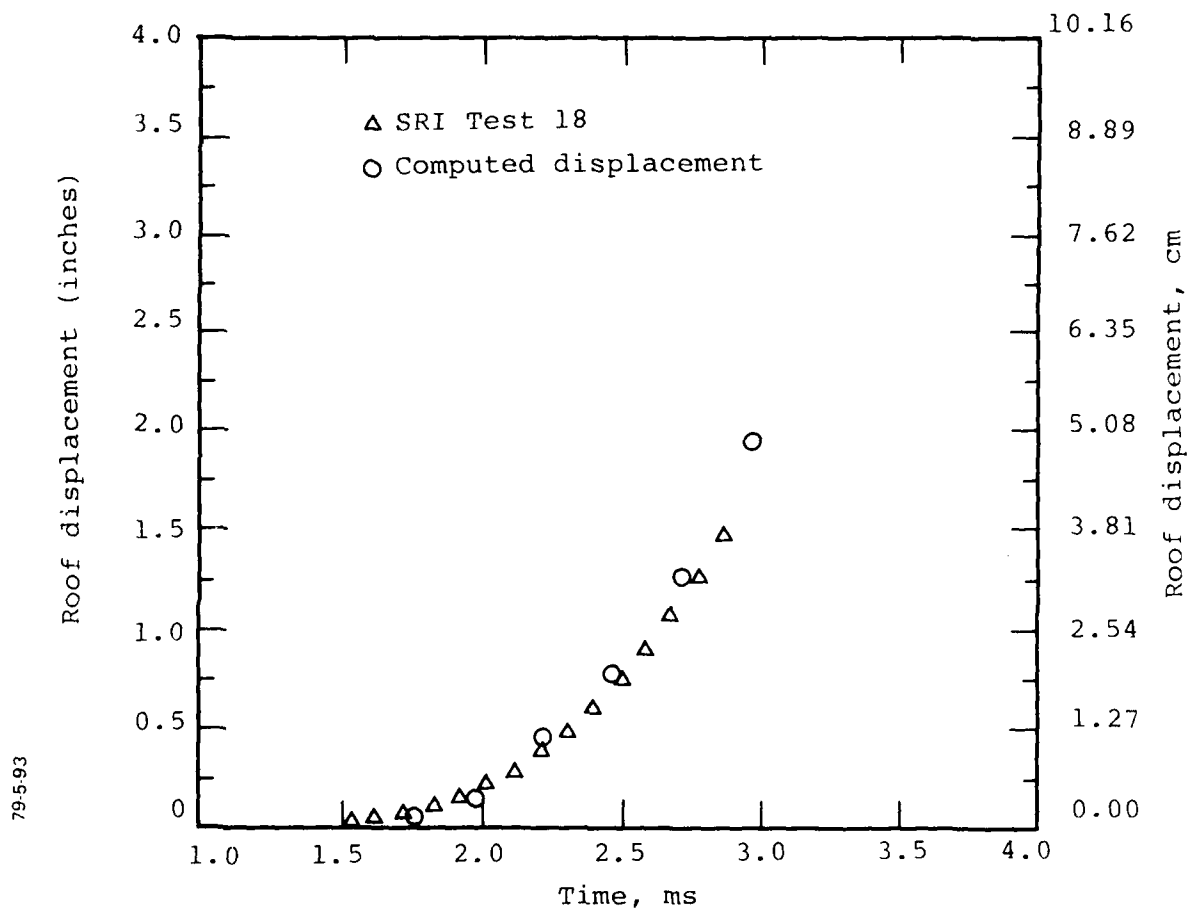
Figure 35   Comparison of computed and measured roof
displacement histories at the reflecting wall,
SRI Test 18 (Pin 1 position).

65

4.0

3.5   ▼ SRI Test 18

○ Computed displacement

3.0

2.5

Wall displacement (inches)

2.0

1.5

1.0

0.5

0

79-5-94

1.0   1.5   2.0   2.5   3.0   3.5   4.0

Time, ms

10.16

8.89

7.62

6.35

5.08

3.81

2.54

1.27

0.00

Wall displacement, cm

10.

Figure 36   Comparison of computed and measured wall displacement
histories at the reflecting wall, SRI Test 18.

66

Figure 37   Computed pressure profiles in the trench at
             various times, SRI Test 18, (Solid line:with
             venting, Dashed line: without venting).

SECTION 6

SUMMARY

Calculations were performed corresponding to Tests 11, 17 and 18 of the SRI "Laboratory Investigations of the Expansion and Venting of the MX Trench" program. The calculations were performed to compare the theoretical and experimental results in detail and thus assess the capability of the theoretical models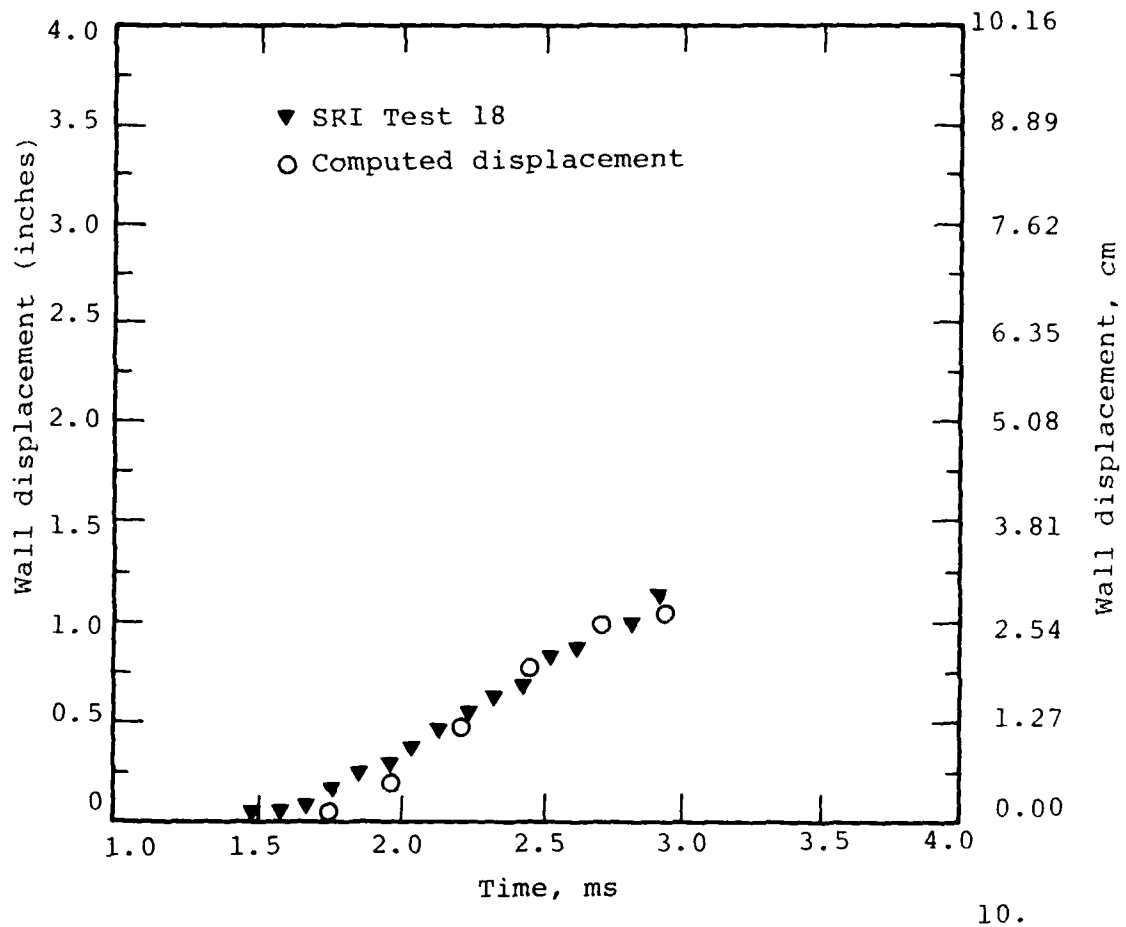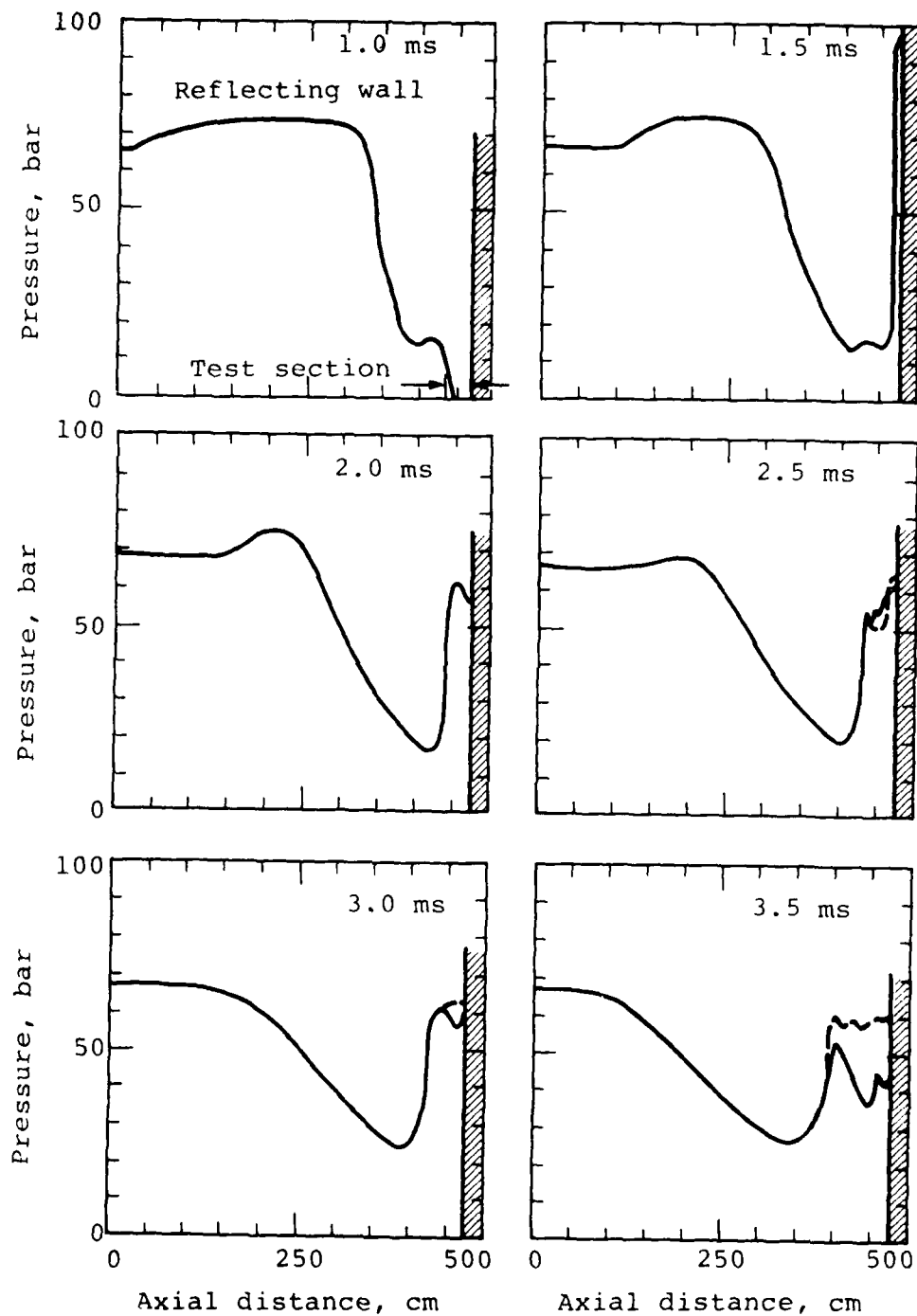 to reproduce the essential features of the trench expansion and venting process under the conditions achieved in the experiments. A further objective was to use the experimental data itself as well as the correlations between the theoretical results and the experimental data to provide insight for developing improved models of the trench expansion and venting process.

SRI Test 11 exhibited no venting of the trench gases to the atmosphere and so no venting model was incorporated into the calculations. The computed and measured pressure histories at the reflecting wall for Test 11 are in reasonably good agreement. This supports the use of simple inertial models for computing trench expansion.

Based on analysis of the SRI experimental data and the results of a number of preliminary calculations (not reported here), a new model for trench venting was developed and is proposed for consideration. The advantage of this somewhat empirical model is that it provides a means of calculating the venting time of the trench gases to the atmosphere when only the pressure and density of the in-trench gas and the density and

thickness of the soil overburden are known. The venting model assumes a single crack near the crown of the trench. In-trench gas flows through this crown crack, forming a gas jet. Simple jet penetration theory is used to calculate the time required for the gas jet to penetrate the soil overburden. Venting of the trench gases to the atmosphere is then initiated. Actual venting of the trench gases to the atmosphere is modeled as critical orifice flow through a time-dependent flow area.

The trench venting model was used in the calculations for SRI Tests 17 and 18 (Test 11 did not vent). For Test 17, the jet penetration model predicted the onset of venting at the reflecting wall about 1.1 ms after shock arrival. High speed photography from the experiment suggested that venting did not begin until about 2.4 ms after shock arrival. The experimental pressure histories for Test 17 appear to be consistent with venting beginning about 1.3 ms after shock arrival, when compared with the Test 11 (no vent) data. In short, although the computed and measured pressure histories in the trench agree very well for Test 17, it is uncertain whether this experiment can be used as a basis for assessing the proposed venting model because of the disagreement in the vent time.

The jet penetration model predicted venting to begin at the reflecting wall about 1.1 ms after shock arrival for Test 18. The experimentally observed time of venting is 1.2 ms after shock arrival, in good agreement with this theoretical prediction. The computed and measured pressure histories in the trench are also in good agreement for Test 18 and these results tend to support the proposed venting model.

Additional calculations and analysis will be required to fully evaluate the venting model. Of particular interest is how

69

well the model will work at the higher in-trench pressures of primary interest. In assessing the venting model, it must also be remembered that even under seemingly well-controlled conditions there appears to be a relatively high degree of variability in the venting process. This is illustrated by the results of SRI Tests 18, 19, and 20 (Reference 1). These three experiments were nominally identical; however, the onset of venting in these experiments varied from 1.2 ms (Tests 18 and 19) to 1.8 ms (Test 20) after shock arrival at the reflecting wall.

The SRI experiments have provided a very good data base against which theoretical models of MX trench expansion and venting can be assessed for relatively low in-trench pressures. The good overall agreement between these data and the theoretical results reported here is an encouraging first step in developing theoretical venting models to compute venting in the MX trench.

REFERENCES

1. J. R. Bruce and J. K. Gran, "Laboratory Investigations of the Expansion and Venting of the MX Trench," DNA Report DNA4625F (1978).

2. Personal communication for J. R. Bruce, SRI International, Menlo Park, CA.

3. E. L. Lee, H. C. Hornig and J. W. Kury, "Adiabatic Expansion of High Explosive Detonation Products," UCRL-50422, Lawrence Radiation Laboratory, Livermore, CA., May, 1968.

4. Y. C. Fung, Foundations of Solid Mechanics, Prentice Hall, New York, N.Y., 1965.

5. G. Birkhoff, D. P. MacDougall, E. M. Pugh and Sir G. Taylor, "Explosives with Lined Cavities," J. Appl. Phys., 19, pp. 563-82, 1948.

6. L. D. Landau and E. M. Lifshitz, Fluid Mechanics, Addison-Wesley, New York, N.Y., 1959.

7. J. R. Bruce, "Laboratory Investigations of Expansion and Venting of the MX Trench-Progress Report No. 1," SRI International, Menlo Park, CA., 30 June 1977.

DISTRIBUTION LIST

DEPARTMENT OF DEFENSE

Assistant to the Secretary of Defense
Atomic Energy
    ATTN: Executive Assistant

Defense Advanced Rsch. Proj. Agency
    ATTN: TIO

Defense Intelligence Agency
    ATTN: RDS-3A

Defense Nuclear Agency
    ATTN: SPSS, G. Ullrich
    ATTN: SPSS, E. Sevin
    ATTN: DDST
3 cy ATTN: SPSS, J. Galloway
4 cy ATTN: TITL

Defense Technical Information Center
12 cy ATTN: DD

Field Command
Defense Nuclear Agency
    ATTN: FCPR
    ATTN: FCTMD

Field Command
Defense Nuclear Agency
Livermore Division
    ATTN: FCPRL

Joint Strat. Tgt. Planning Staff
    ATTN: NRI-STINFO Library
    ATTN: XPFS

Undersecretary of Defense for Rsch. & Engrg.
    ATTN: Strategic & Space Systems (OS)

DEPARTMENT OF THE ARMY

BMD Advanced Technology Center
Department of the Army
    ATTN: ATC-T

Chief of Engineers
Department of the Army
    ATTN: DAEN-ASI-L
    ATTN: DAEN-MPE-T, D. Reynolds
    ATTN: DAEN-RDL
    ATTN: DAEN-RDM

Harry Diamond Laboratories
Department of the Army
    ATTN: DELHD-N-P
    ATTN: DELHD-I-TL

U.S. Army Ballistic Research Labs.
    ATTN: DRDAR-TSB-S
    ATTN: DRDAR-BLE, J. Keefer

U.S. Army Cold Region Res. Engr. Lab.
    ATTN: Library

U.S. Army Construction Engrg. Res. Lab.
    ATTN: Library

DEPARTMENT OF THE ARMY (Continued)

U.S. Army Engineer Center
    ATTN: Technical Library

U.S. Army Engr. Waterways Exper. Station
    ATTN: WESSA, W. Flathau
    ATTN: Library
    ATTN: WESSD, G. Jackson

U.S. Army Material & Mechanics Rsch. Ctr.
    ATTN: Technical Library

U.S. Army Materiel Dev. & Readiness Cmd.
    ATTN: DRXAM-TL

U.S. Army Nuclear & Chemical Agency
    ATTN: Library

DEPARTMENT OF THE NAVY

Naval Construction Battalion Center
    ATTN: Code L53, J. Forrest
    ATTN: Code L08A
    ATTN: Code L51, J. Crawford

Naval Facilities Engineering Command
    ATTN: Code 09M22C

Naval Postgraduate School
    ATTN: G. Lindsay
    ATTN: Code 0142

Naval Research Laboratory
    ATTN: Code 2627

Naval Surface Weapons Center
    ATTN: Code X211
    ATTN: Code F31

Naval Surface Weapons Center
    ATTN: Tech. Library & Info. Services Branch

Office of Naval Research
    ATTN: Code 715

DEPARTMENT OF THE AIR FORCE

Air Force Institute of Technology
    ATTN: Library

Air Force Systems Command
    ATTN: DLWM

Air Force Weapons Laboratory
Air Force Systems Command
    ATTN: DEY
    ATTN: DES-G
    ATTN: DEO
    ATTN: SUL
    ATTN: DE, M. Plamondon
    ATTN: DES-S
    ATTN: NT, D. Payton
    ATTN: DED-A
    ATTN: DED-I

DEPARTMENT OF THE AIR FORCE (Continued)

Assistant Chief of Staff
Intelligence
Department of the Air Force
    ATTN: IN

Assistant Secretary of the Air Force
Research, Development & Logistics
    ATTN: SAFALR/DEP for Strat. & Space Sys.

Ballistic Missile Office
Air Force Systems Command
    ATTN: MNNXH, D. Gage
    ATTN: MNNX, W. Crabtree

Deputy Chief of Staff
Research, Development, & Acq.
Department of the Air Force
    ATTN: AFRDQA
    ATTN: AFRDPN
    ATTN: AFRDQSM
    ATTN: AFRD-M, L. Montulli

Strategic Air Command
Department of the Air Force
    ATTN: NRI-STINFO Library
    ATTN: XPFS

Vela Seismological Center
Department of the Air Force
    ATTN: G. Ullrich

DEPARTMENT OF ENERGY CONTRACTORS

Lawrence Livermore Laboratory
    ATTN: Document Control for D. Glenn

Los Alamos Scientific Laboratory
    ATTN: Document Control for C. Keller
    ATTN: Document Control for R. Sanford

Sandia Laboratories
    ATTN: Document Control for Org. 1250, W. Brown
    ATTN: Document Control for A. Chabai

OTHER GOVERNMENT AGENCY

Federal Emergency Management Agency
    ATTN: Hazard Eval. & Vul. Red. Div.,
        G. Sisson

DEPARTMENT OF DEFENSE CONTRACTORS

Acurex Corp.
    ATTN: C. Wolf
    ATTN: K. Triebes
    ATTN: J. Stockton

Aerospace Corp.
    ATTN: H. Mirels
    ATTN: Technical Information Services

Agbabian Associates
    ATTN: M. Agbabian

Applied Theory, Inc.
2 cy ATTN: J. Trulio

Boeing Co.
    ATTN: Aerospace Library
    ATTN: S. Strack

DEPARTMENT OF DEFENSE CONTRACTORS (Continued)

California Research & Technology, Inc.
    ATTN: Library
    ATTN: M. Rosenblatt

Civil Systems, Inc.
    ATTN: J. Bratton

Civil Systems, Inc.
    ATTN: S. Melzer

Eric H. Wang
Civil Engineering Rsch. Fac.
    ATTN: P. Lodde
    ATTN: J. Kovarna

General Electric Company-TEMPO
    ATTN: DASIAC

H-Tech Labs, Inc.
    ATTN: B. Hartenbaum

Higgins, Auld & Associates
    ATTN: N. Higgins
    ATTN: H. Auld

IIT Research Institute
    ATTN: Documents Library

J. H. Wiggins Co., Inc.
    ATTN: J. Collins

Merritt CASES, Inc.
    ATTN: Library

Nathan M. Newmark Consult. Eng. Svcs.
    ATTN: W. Hall
    ATTN: N. Newmark

Pacific-Sierra Research Corp.
    ATTN: H. Brode

Mission Research Corp.
    ATTN: C. Longmire
    ATTN: G. McCartor

Pacifica Technology
    ATTN: Library
    ATTN: R. Allen

Physics International Co.
    ATTN: Technical Library
    ATTN: J. Thomsen
    ATTN: F. Sauer
    ATTN: D. Orphal
    ATTN: M. Chawla
    ATTN: K. Abbott

R & D Associates
    ATTN: J. Carpenter
    ATTN: J. Lewis
    ATTN: C. MacDonald
    ATTN: R. Port
    ATTN: Technical Information Center

Science Applications, Inc.
    ATTN: Technical Library
    ATTN: R Schlaug
    ATTN: H. Wilson